



University  
of Glasgow

Wilson, Chris (2013) *Monophonic and polyphonic acoustic vortices: the foundation of acoustic tweezers*. MSc(R) thesis.

<http://theses.gla.ac.uk/5092/>

Copyright and moral rights for this thesis are retained by the author

A copy can be downloaded for personal non-commercial research or study, without prior permission or charge

This thesis cannot be reproduced or quoted extensively from without first obtaining permission in writing from the Author

The content must not be changed in any way or sold commercially in any format or medium without the formal permission of the Author

When referring to this work, full bibliographic details including the author, title, awarding institution and date of the thesis must be given

# Monophonic and Polyphonic Acoustic Vortices: The Foundation of Acoustic Tweezers

Chris Wilson  
BSc



Submitted in fulfilment of the requirements for  
the Degree of Master of Science

Department of Physics & Astronomy  
Faculty of Physical Sciences  
University of Glasgow

June 2011

*"You can't connect the dots looking forward. You can only connect them looking backwards, so you have to trust that the dots will somehow connect in your future. You have to trust in something - your gut, destiny, life, karma, whatever, because believing that the dots will connect down the road will give you the confidence to follow your heart, even when it leads you off the well-worn path, and that will make all the difference."*

Steve Jobs, CEO, Apple Inc and Pixar Animation,

*2005 Stanford Commencement Address*

---

This thesis is a presentation of my original work. Wherever contributions of others are involved, every effort is made to indicate this clearly, with due reference to the literature, and acknowledgement of collaborative work and discussions.

Signed: \_\_\_\_\_ December 27, 2013

---

# Acknowledgements

Firstly, I'd like to thank Professor Miles Padgett for his guidance throughout the course of my study, also for putting up with my temperamental sleep cycles and ease of distraction. A big thanks to every member of the optics group at the University of Glasgow who has contributed in some way to this thesis, and to my education while there. Thanks also to those group members at who's desk I sat during December 2010/January 2011 while I put the finishing touches to this work.

Thanks also to Jonathan Leach, who is most certainly the badger, for his help both with and regarding the project, without who's sage wisdom and encyclopedic knowledge of LabView this thesis would be considerably lighter.

Finally I'd like to thank my parent for all the support that has lead to this work.

This research is supported by the Engineering and Physical Sciences Research Council (EPSRC), who's funding allowed me to quit Sainsbury's.

# Abstract

It is well known that light is capable of carrying a component of orbital angular momentum (OAM), and that this OAM can be manipulated in such a way as to be useful in applications such as optical trapping, leading to the development of optical tweezers which now see use in many fields for the manipulation of small scale particles. Despite the advances in the field of optical OAM, relatively little research has been conducted in the field of acoustical OAM. Presented in this thesis is evidence of the equivalence of optical and acoustical OAM in several experiments that have already been proven and widely accepted for the optical case.

Demonstrated in chapter 3 is what has been dubbed an *acoustic spanner*, which provides a preamble to the main body of the research. In this chapter, an experiment that demonstrates how sound waves can carry a component of OAM using simple off-the-shelf equipment is discussed. An annular array of loudspeakers was constructed and a set of analogue electronics was assembled in such a way that, when driven by a signal from a laboratory signal generator, eight individual signals were produced, identical to the driving signal, but separated by a relative phase difference of  $\pi/4$ . The net result is that, considered as a set, there is

a difference of  $2\pi$  between the first and eighth signals. These signals were sent to the eight speakers which resulted in an approximation to a  $\ell = 1$  beam. A demonstration is also made of how the OAM carried by a sound beam may be transmitted to matter by observing the rotation of a styrofoam disk, and measure the total displacement from it's equilibrium position. These results were confirmed when the direction of the beam was reversed by reversing the direction of the phase increase.

A further experiment detailed in chapter 4 was conducted where four signals of varying frequency were superimposed upon one another before being phase shifted and sent to the speakers. This meant that instead of a beam with a single tone, as was generated in the acoustic spanner experiment, a polyphonic acoustic vortex was generated using four frequencies. Using a microphone mounted atop a translation stage, an amplitude cross-section of the vortex confirmed that there were indeed four constituent vortices in the beam. It was also confirmed that these constituent beams were not coupled to one another, and thus it was possible to steer each component of the vortex without affecting the others. This was achieved by modulating the amplitude of the signal at one speaker, and applying an equal and opposite modulation at the corresponding speaker on the opposite side of the array.

The final experiment was an investigation into the phase structure of acoustical vortices. While only first order beams were used in the acoustic spanner and polyphonic vortex experiments, high order beams were produced this time. Beams of  $\ell = \pm 1 \pm 2 \pm 4$  were produced, and the same microphone and translation stage that was used before was used to

trace a 2-dimensional cross-section through the beams and measure their phase profiles. The results for  $\ell = \pm 1$  and  $\pm 2$  were as expected, and the phase profiles for these can be seen in the figures in chapter 5. Beams for  $\ell = \pm 4$  were expected to fail since the number of speakers used in the array did not provide enough sources for the beam to fully form into a vortex, and this was also as expected. The phase profiles are included in chapter 5 to demonstrate the limitations of the experiment, and to show that in this case that it's impossible to differentiate between a  $\ell = 4$  and a  $\ell = -4$  beam in the way that can be done for the others. Similarly,  $\ell = \pm 3$  beams are not measured due to the limitations of the apparatus.

# Contents

|   |     |
|---|-----|
| <b>Contents</b>   | i   |
| <b>List of Figures</b>  | iii |
| <b>List of Tables</b>   | x   |
| <b>1 Introduction</b>   | 1   |
| 1.1 An overview of this thesis . . . . .  | 1   |
| 1.2 From optics to acoustics to optics to acoustics: a brief history of vortex research . . . . . | 3   |
| 1.3 A conceptual and mathematical analysis of vortices in acoustic waves . . . . .                | 4   |
| <b>2 Experimental apparatus</b>   | 18  |
| 2.1 Generating and detecting the vortices . . . . .   | 20  |
| 2.2 Acoustic spanner . . . . .  | 25  |
| 2.3 Polyphonic vortex . . . . .   | 29  |
| <b>3 An acoustic spanner and its associated rotational Doppler shift</b>                          | 31  |
| 3.1 Introduction . . . . .  | 31  |

|  |           |
|--|-----------|
| 3.2 Generating helically phased acoustic beams . . . . .           | 34        |
| 3.3 Acoustic spanner . . . . .                                     | 35        |
| 3.4 Rotational Doppler Shift . . . . .                             | 39        |
| <b>4 A polyphonic acoustic vortex and its complementary chords</b> | <b>43</b> |
| 4.1 Introduction . . . . .   | 43        |
| 4.2 Apparatus . . . . .  | 48        |
| 4.3 The Experiment . . . . .                                       | 50        |
| <b>5 Phase structures of high-order acoustic vortex beams</b>      | <b>60</b> |
| 5.1 Introduction . . . . .   | 60        |
| 5.2 High order optical beams . . . . .                             | 62        |
| 5.3 Techniques for generating high-order L-G optical beams . .     | 63        |
| 5.4 Higher order acoustical beams . . . . .                        | 68        |
| <b>6 Conclusions</b>   | <b>77</b> |
| <b>Publications</b>  | <b>81</b> |
| <b>Bibliography</b>  | <b>82</b> |

# List of Figures

|   |    |
|---|----|
| 1.2 Two separate illustrations of the wave trains A and B, traveling in different directions and oriented at an angle to one another, as they interfere. Note that the normal of each wave make an angle $\alpha$ with the $O_z$ axis. The bold lines indicate that the wave in question predominates in that particular region. It can be seen from these figures that wave A predominates below the $O_x$ axis while wave B predominates above the axis. Figure 1.2a illustrates this for the case where both wave fronts are symmetrical, and figure 1.2b illustrates the anti-symmetrical case. . . . .   | 9  |
| 1.3 Argand diagrams illustrating the complex wave function at four separate points in the vicinity of a dislocation. Figure 1.3a represents the complex wave function as measured from point P, and as the receiver is moved from P to R, the diagram gradually changes to that shown in 1.3d. This transition can only be possible if, at some point during the transition, the curves passes through the origin, at which point $\psi_c$ and $\psi_s$ , and subsequently $\rho$ , are reduced to zero. This is further verification that a dislocation exists at the point during the transition at which the curve passes through zero, as can be seen in 1.3c, while the figure shown in ?? is representative of a measurement made at some position between positions P and Q. . . . . | 11 |

|   |    |
|---|----|
| 1.4 Two monochromatic plane waves, A and B traveling at different orientations to the x-axis, interfere at an angle to one another. This results in a set of parallel screw dislocations in a plane parallel to the $O_z$ axis. . . . .   | 14 |
| 2.1 Photograph of the experimental setup for the polyphonic vortex experiment (see chapter 4). Seen in the picture is the enclosure that housed the speakers (item 1), the translation stage to which the microphone was attached (item 2) and the digital sound card and amplifier deck (item 3). Item 1, in its current form, has been a part of the setup from the beginning. Item 2 was originally a styrofoam disk suspended from a mount high above the experiment, which was used for the acoustic spanner experiment, and was then replaced with a microphone attached to the translation stage for the polyphonic vortex and phase profile experiments. Item 3, the digital sound card and amplifier deck, was added to the setup in order to replace the analogue circuitry that was used in the acoustic spanner experiment in chapter 3 . . . . . | 19 |
| 2.2 The circular array of loudspeakers used in all three experiments, with the microphone used in the polyphonic vortex and phase profile experiments seen suspended in the centre of the array. It should be noted that despite there being sixteen speakers shown in the figure, only eight, every alternating one, was connected. . . . .  | 20 |

|      |  |    |
|------|--|----|
| 2.3  | Translation stage with attached microphone. The microphone was held stationary for the quantum core experiment, and the stage was added later in order to take 2-dimensional scans of the polyphonic vortex. . . . . | 22 |
| 2.4  | The enclosure containing the speaker array. The grey material on the interior and exterior walls is lead lined foam that was applied in order to increase the acoustic insulation. . . . .                           | 23 |
| 2.5  | A styrofoam disk suspended above the speaker array. The grey objects are weights that were applied in order to balance the disk. A schematic of this arrangement may be seen in figure 2.6                           | 24 |
| 2.6  | A styrofoam disk suspended above the speaker array. A physical example of this may be seen in figure 2.5. . . . .  | 25 |
| 2.7  | An illustration of the acoustic spanner experiment. . . . .  | 26 |
| 2.8  | An illustration of the measurement of the rotational Doppler shift of the acoustic spanner, . . . . .  | 27 |
| 2.9  | An illustration of the polyphonic vortex experiment. . . . .   | 28 |
| 2.10 | An illustration of the measurement of the polyphonic acoustic vortex. . . . .  | 29 |
| 2.11 | Motu 828mkIII digital sound card. . . . .  | 30 |

|   |    |
|---|----|
| 3.1 Comparison of the motion of the pendulum calculated from the equation of motion and the observed angular displacement. The parameters for damping and stiffness constant are deduced from observation and the resulting agreement between predicted and observed motion is good. Measurements of torque can be deduced from $\alpha_i$ ( $\Gamma_s = I\alpha_i$ ) or T and $\theta_{max}$ ( $\Gamma_s = 4\pi I\theta_{max}/T^2$ ). . . . . .      | 36 |
| 3.2 Measurements of the sound level across the diameter of the containment cylinder at the position of the acoustic tile (0.15m height above the loudspeakers) and the plane where Doppler results were taken (approximately 0.8m above the loudspeakers). Each trace represents an average of several traverse scans with a roaming microphone. . . . .  | 40 |
| 3.3 Results of the rotational Doppler effect measured with a spinning microphone. The frequency offset in Hz, $\Delta f_z$ , is equal to the revolutions per second made by the microphone relative to the source (or $\omega_t/2\pi$ , where $\omega_r$ is the relative angular velocity). The downshifted frequency corresponds to the case when the microphone is rotated in the direction of increasing phase of the helical phase front. . . . . | 42 |

|     |  |    |
|-----|--|----|
| 4.1 | Amplitude cross-section through the acoustic vortex at 523 Hz, recorded for three different sound volumes. The points are the experimentally recorded data and the solid lines are linear best fits (not constrained to pass through zero), and the horizontal arrows mark the extent over which the noise of the measurement system dominates over the measured signal. . . . . | 44 |
| 4.2 | 2D plots of amplitudes corresponding to the four frequency components of the polyphonic acoustic vortex. Note that the singularities all overlap in the centre of the beam. . . . .  | 45 |
| 4.3 | Amplitude cross-section of the polyphonic vortex recorded at much higher volume than shown in figure. 4.1. The points show the experimental data and the solid line shows the best linear fit. (a) and (b) indicate the off and on-axis positions for which the full spectral signals are shown in figures 4.4 and 4.5.  | 46 |
| 4.4 | Spectral plots of the microphone signal recorded at the off (a) axis positions of figure 4.3. . . . .  | 47 |
| 4.5 | Spectral plots of the microphone signal recorded at the on (b) axis position of figure 4.3. . . . .  | 50 |
| 4.6 | Perturbation of the vortex components. The four arrows indicate the positions of the complementary chords of the vortex, and a spectral analysis was made of each point. The results of this analysis can be seen in figures 4.8 to 4.11. . . .  | 52 |
| 4.7 | Polyphonic vortex algorithm . . . . .  | 53 |
| 4.8 | Spectral plot of the suppression of the 523 Hz component. . .  | 55 |
| 4.9 | Spectral plot of the suppression of the 440 Hz component. . .  | 56 |

|   |    |
|---|----|
| 4.10 Spectral plot of the suppression of the 392 Hz component. . . . .  | 57 |
| 4.11 Spectral plot of the suppression of the 329 Hz component. . . . .  | 58 |
| 5.1 A sketch of a spiral phase plate . . . . .  | 62 |
| 5.2 A wrapped phase map indicating the phase value measured at<br>each speaker for each value of $\ell$ . . . . . | 64 |
| 5.3 An $\ell = 1$ beam. . . . .   | 66 |
| 5.4 An $\ell = -1$ beam. . . . .  | 67 |
| 5.5 An $\ell = 2$ beam . . . . .  | 69 |
| 5.6 An $\ell = -2$ beam . . . . .   | 71 |
| 5.7 A $\ell = 4$ beam . . . . .   | 73 |
| 5.8 A $\ell = -4$ beam . . . . .  | 75 |

# List of Tables

- 3.1 Summary of acoustic spanner results. Torque values are shown for the methods described in the text, using the initial and long-term parts of the observed motion. Ideally, for a given acoustic set-up, we would expect the torque to be independent of suspension wire radius and comparable to the value measured from the properties of the acoustic beam (estimated to be  $6.4 \times 10^{-6}$  Nm). . . . . 38

# CHAPTER

1

## Introduction

### 1.1 An overview of this thesis

Over the past few years, a considerable amount of research has been carried out on the phenomena of optical orbital angular momentum, which has lead to the development of devices such as optical tweezers and spanners, as well as providing the fundamental concepts that underly the current research into quantum information protocols, as well as the technology that will utilize them. It is therefore difficult to argue against the usefulness of such research and the benefits that these technologies will one day provide. It is subsequently a great irony that the original paper that initiated this work was not an optical paper, but was in fact an acoustic paper, published in 1974 by Nye and Berry who were attempting to understand the origin of strange anomalies that were observed in radio echoes reflecting off the bottom of the Antarctic ice sheet. Since then, very little work has been carried out on the subject of acoustic

phase singularities, rather the optical phenomena have been the primary focus of research. This thesis is intended to demonstrate the ease with which ideas that have been demonstrated in the optical field may also be applied to the acoustic regime, and this introductory chapter aims to review existing literature on helically phase acoustic beams.

Chapter 3, entitled *An acoustic spanner and it's associated rotational Doppler shift*, provides a background to the work carried out for this thesis. The experiment described therein was carried out before commencement of formal studies by the author and is provided for contextual purposes. The acoustic spanner was developed and demonstrated based on ideas developed in a paper published to detail the invention of an optical spanner. While the difference between optical and acoustical waves is fundamental, it is demonstrated that it is possible to transfer orbital angular momentum from an acoustic wave to matter, as has previously been demonstrated for optical waves.

Chapter 4, which is entitled *A polyphonic acoustic vortex and it's complimentary chords*, details the experiment that resulted in a publication in *New Journal of Physics*. In this experiment, a polyphonic acoustic vortex is generated by using a digital sound card to produce four independent wave trains of differing frequency, and superimpose them atop one another. This signal was then sent to the same circular speaker array used to produce the acoustic spanner. The four original signals generated by the sound card are each perturbed by different amounts, resulting in the relative displacement of each singularity with respect to the others. A scan of the cross-section of the resulting sound

field verified that, at each singularity, the other three were still audible, and each of these points has been dubbed a *complimentary chord* of the polyphonic vortex.

## 1.2 From optics to acoustics to optics to acoustics: a brief history of vortex research

The first suggestion that a wave could carry a component of momentum came in 1909 when Poynting [1] proposed that a circularly polarised beam of light incident upon a line of particles lying parallel to the beam axis would be left in a spiral formation upon the beams passing. He proposed that this phenomena was the result of light of that polarisation carrying a component of angular momentum, and this hypothesis was later verified by Beth [2] in 1936. This component of angular momentum has since been identified as the spin angular momentum, and today such beams can be generated by simply placing a spiral phase plate in their path of propagation.

After Beth's confirmation of Poynting's prediction, it wasn't until 1974 that the concept of a vortex in a wave field was proposed. Nye and Berry [3], while investigating the structure of reflections from the bottom of the Antarctic ice sheet of ultrasonic waves, noticed that the reflected wave trains contained regions where the signal was reduced to zero. These dislocations, also referred to as vortices, have since formed the

basis of an entire field of optics and in 1992, Allen[4] *et al* combined the results of Poynting/Beth and Nye and demonstrated the transfer of the orbital angular momentum component of a polarised beam of laser light from the beam into matter. Another paper published that same year by Ceperley [5] provided a detailed description of rotating wave fields where they were raised to the same level of significance of travelling and standing waves.

Recently, two experiments [6, 7] were carried out to recreate the effect described by Allen in 1992 using acoustic vortices. Both experiments were successful, with both parties, only being made aware of each others existence during the later stages of both of their projects. Both experiments resulted in publications that paved the way for the work in this thesis [8].

### 1.3 A conceptual and mathematical analysis of vortices in acoustic waves

In their seminal paper [3] in 1974, Nye and Berry describe theoretically the effect of edge, screw, and mixed edge-screw dislocations in trains of waves that propagate in different directions and subsequently interfere. They used the example of ultra-sonic waves being reflected from a rough surface in air. Their work originated from an attempt to understand the radio echoes that were detected after a signal was sent through the Antarctic ice sheet. Screw dislocations, are otherwise known as

vortices. An experiment was set up in a laboratory environment, with the radio waves being replaced with ultra-sound as the relatively low frequency of these waves allowed for highly detailed study of the echoes. A pulse consisting of 10 sinusoidal waves, each of approximately 100kHz contained within a smoothly varying Gaussian envelope. The echo signal that was detected from the rough surface consisted of approximately 50 sinusoidal waves in an envelope of fluctuating amplitude. Moving the microphone along a line revealed several points at which the pulse had zero amplitude for a duration of time.

This observation was only made possible by using a pulsed signal, rather than a monochromatic one. Any point within a monochromatic wave must be sinusoidal, and there must also be a periodicity to the wave if a dislocation is to be identified. Thus, dislocations are structures that require both the localization property of a pulse and the oscillation property of a continuous wave; and that disappear at both the monochromatic and white noise limit. There are however exceptions to these rules, one being the non-localized interference fringe as produced by the Young's two slit experiment. Others include stationary pure dislocations, and localized interference fringes. The paper focused simply on an analysis and description of the dislocations, pointing out that they are to be expected whenever pulses from a common oscillator are interfered with one another, and the method by which they are produced is covered in a separate publication.

## Edge dislocations

Consider the complex wave function

$$\psi(t) = \psi_c(t) + i\psi_s(t) = \rho(t)e^{i\chi(t)} \quad (1.1)$$

where  $\chi$  is real and  $\rho$  is both real and positive. Then

$$\rho^2(t) = \psi_s^2(t) + \psi_s^2 \quad (1.2)$$

where  $\rho(t)$  is positive, and

$$\tan\chi(t) = \frac{\psi_s(t)}{\psi_c(t)} \quad (1.3)$$

From the above, we can define  $\rho(t)$  and  $\chi(t)$  as the amplitude and phase respectively of the wave. With this definition,  $\rho(t)$  is the envelope of the observed oscillation as the phase of the original is varied. This variation in the original phase is essential in order to obtain complete phase and amplitude information as  $\rho(t)$  is not strictly deducible by observing a single instance of the signal.

An illustration of the formation of an edge dislocation can be seen in figure 1.1<sup>1</sup>. An observation made from point P by a receiver positioned directly in the path of an encroaching wavefront will reveal a number of crests, in this case 6. Consider only the wave fronts A and C. The receiver used to make this observation is swept from point P to point R, and in doing so, it is noticed that another crest is formed, crest B. This is observed to happen as the receiver passes point Q. The amplitude of crest B drops to zero at point N. If the wavefront is considered in

---

<sup>1</sup>Figure attributed to *Dislocations in Wave Trains*, 1974, doi: 10.1098/rspa.1974.0012

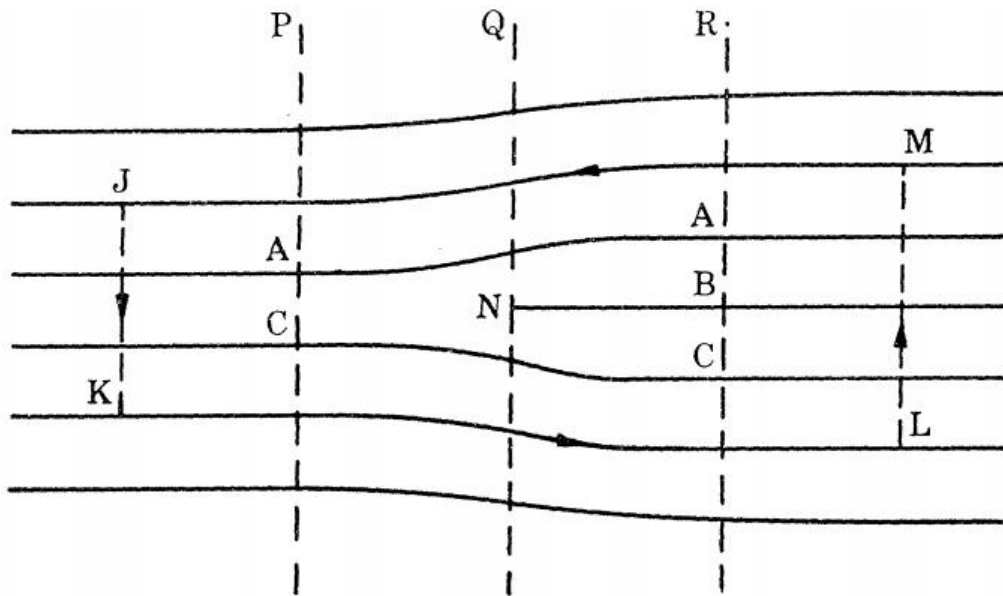


Figure 1.1: An illustration of the formation of a dislocation. An observer at point P will observe the wave crest AC as it propagates through time and space. A subsequent observation made at point Q will reveal the crest to be interacting with an obstacle of some description, and the dislocation is formed at point N, where the wave amplitude falls to zero. This dislocation leads to the formation of a third crest B, observed at point R. The circuit JKLM is known as a 'Burgers Circuit', and in following this circuit, one can ascertain that a dislocation is indeed present in the wave field by counting the number of crests crossed on each pass of the field.

three dimensions, a line of zero intensity would be observed intersecting point N and running parallel to the direction of propagation of the wavefront with crest B terminating at this line. It is for this reason that this phenomena is referred to as an edge dislocation. The existence of a dislocation at point N can be verified by following the circuit LMJK, and by counting the number of crests during the circuit. If the number of crests counted while crossing in one direction does not match the number counted while crossing in the other, then it can be safely assumed that a

dislocation has been enclosed inside.

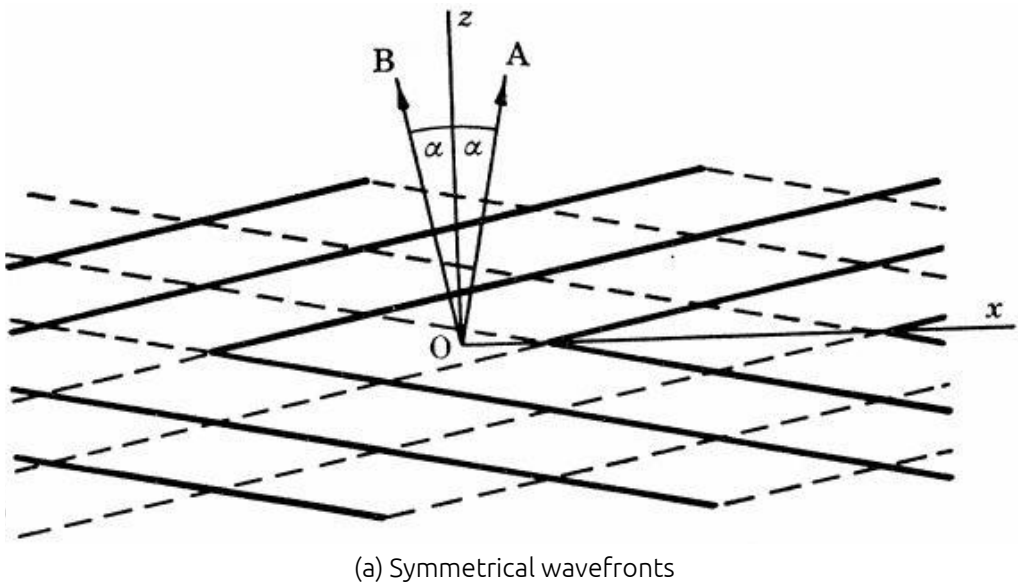
Figure 1.2<sup>2</sup> depicts two situations in which two wave trains, travelling in different directions and at an angle to one another, intersect, producing an interference pattern as they do so. The two scenarios are for symmetric wave fronts (figure 1.2a), and anti-symmetric wave fronts (figure 1.2b). In the symmetric case, the crests of A and B are of equal amplitude when they meet along the  $O_x$  axis, leading to a situation in which wave A predominates below the  $O_x$  axis while wave B predominates in the upper half. In the anti-symmetric case however, the waves meet along the  $O_x$  axis such that a crest of B falls upon a trough of A, resulting in the cancelation of both wave components and the formation of a point of null intensity, or a dislocation. A pattern of such dislocations can be seen along the  $O_x$  axis, marked by dashes oriented perpendicularly to the axis along which the wave fronts are travelling.

Now consider an Argand diagram whose axes are  $\psi_c$  and  $\psi_s$ . The changing complex wave function in equation 1.1 can be represented as a moving point P on this diagram which will encircle the origin quasi-periodically, due to the quasichromaticity of the source, at a frequency of  $2\pi/\omega$ . Figure 1.3<sup>3</sup> depicts four such diagrams that illustrate the behavior of the complex wave function at four positions on and/or between positions P and R. Figure 1.3a illustrates the behavior of the wave function at position P as the crests A and C pass over the receiver. As the receiver is traversed from P to R, the curve changes from the

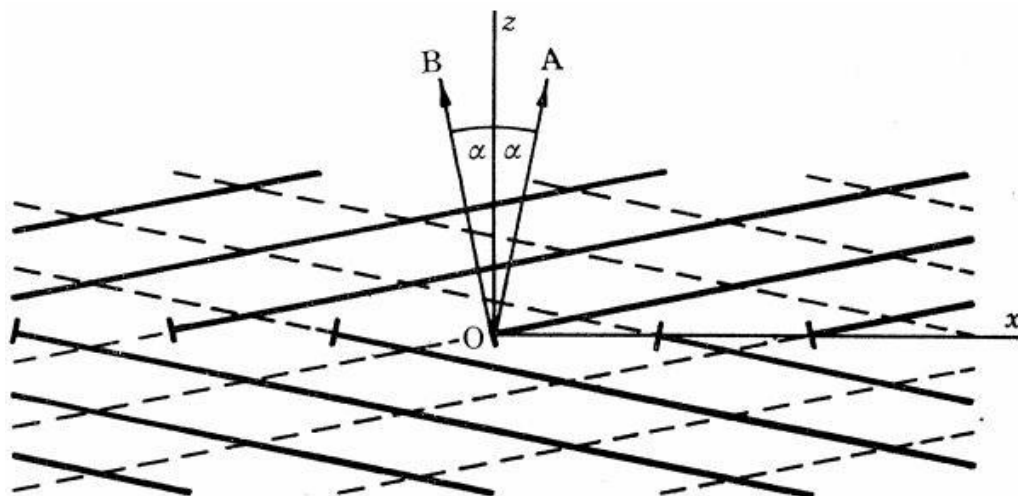
---

<sup>2</sup>Figure attributed to *Dislocations in Wave Trains*, 1974, doi: 10.1098/rspa.1974.0012

<sup>3</sup>Figure attributed to *Dislocations in Wave Trains*, 1974, doi: 10.1098/rspa.1974.0012



(a) Symmetrical wavefronts



(b) Anti-symmetrical wavefronts

Figure 1.2: Two separate illustrations of the wave trains  $A$  and  $B$ , traveling in different directions and oriented at an angle to one another, as they interfere. Note that the normal of each wave make an angle  $\alpha$  with the  $O_z$  axis. The bold lines indicate that the wave in question predominates in that particular region. It can be seen from these figures that wave  $A$  predominates below the  $O_x$  axis while wave  $B$  predominates above the axis. Figure 1.2a illustrates this for the case where both wave fronts are symmetrical, and figure 1.2b illustrates the anti-symmetrical case.

one shown in 1.3a to that shown in 1.3d. At some point during this transition, if a dislocation exists at some place on the path PR, the curve will pass through the origin. This behavior can be seen in figure 1.3c, which illustrates the behavior of the complex wave function at position Q, while figure 1.3b is a measurement taken at some point between P and Q. Consider the waves A and B described above, and let us describe them mathematically as:

$$\begin{aligned}\psi_A &= a_0[1 - \beta_0(k_1x + k_3z - \omega t) + \beta_s k_1 y] \dots \\ &\quad \exp[i(k_1x + k_3z - \omega t - \frac{1}{2}\pi)] \\ \psi_B &= a_0[1 - \beta_0(-k_1x + k_3z - \omega t) - \beta_s k_1 y] \dots \\ &\quad \exp[i(-k_1x + k_3z - \omega t + \frac{1}{2}\pi)]\end{aligned}\tag{1.4}$$

where  $\omega/k = c$ ,  $k_1 = ksina$ ,  $k_3 = kcosa$ ,  $a_0$  and  $\beta_s$  constants,  $\omega$  is the fixed angular frequency of the original oscillator generating these waves,  $k$  is the wave number that corresponds to  $\omega$ , and  $\alpha$  is the angle between the wave normals and the  $z$ -axis. An illustration of these wave as they interfere with one another may be observed in figure ??<sup>4</sup>. These complex wave function satisfy the scalar wave equation

$$c^2 \nabla^2 \psi = \frac{\partial^2 \psi}{\partial t^2}\tag{1.5}$$

where the wave velocity  $c$  is a constant. We now set

$$\begin{aligned}\zeta &= k_1 x \\ \xi &= k_3 z - \omega t\end{aligned}\tag{1.6}$$

---

<sup>4</sup>Figure attributed to *Dislocations in Wave Trains*, 1974, doi: 10.1098/rspa.1974.0012

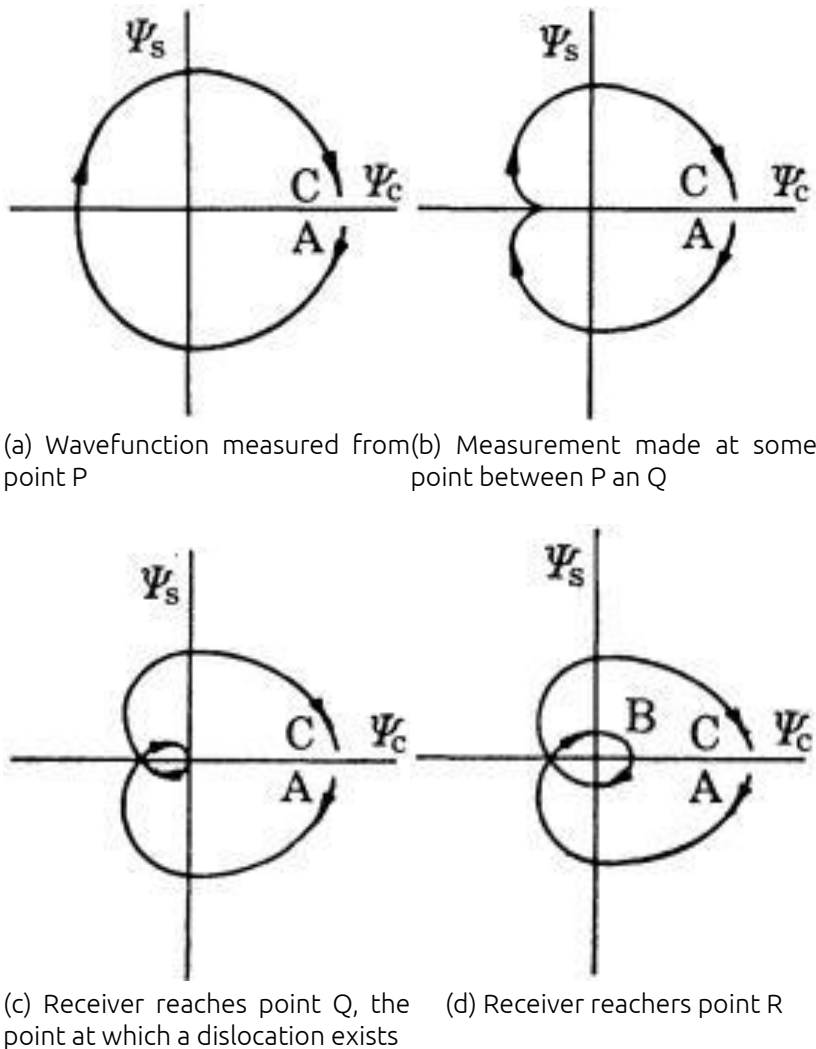


Figure 1.3: Argand diagrams illustrating the complex wave function at four separate points in the vicinity of a dislocation. Figure 1.3a represents the complex wave function as measured from point P, and as the receiver is moved from P to R, the diagram gradually changes to that shown in 1.3d. This transition can only be possible if, at some point during the transition, the curves pass through the origin, at which point  $\psi_c$  and  $\psi_s$ , and subsequently  $\rho$ , are reduced to zero. This is further verification that a dislocation exists at the point during the transition at which the curve passes through zero, as can be seen in 1.3c, while the figure shown in ?? is representative of a measurement made at some position between positions P and Q.

This allows us to rewrite the complex interference

$$\psi = \psi_A + \psi_B \equiv \rho e^{i\chi} \quad (1.7)$$

in terms of  $\xi$  and  $\zeta$ , and thus to redefine the amplitude and phase accordingly as

$$\rho^2 = 4a_0^2((1 - \beta_e\xi)^2 \sin^2 \xi + (\beta_e\zeta)^2 \cos^2 \xi) \quad (1.8)$$

and

$$\chi = \arctan\left(\frac{\beta_e\zeta}{(1 - \beta_e\xi)\tan\xi}\right) + \zeta + 2n\pi \quad (1.9)$$

If an integer value of  $n$  is chosen that results in  $\chi$  lying in the region  $\pm\pi$ , then  $\chi$  will become  $\chi_0$ , and shall be referred to as the reduced phase. Any other value of  $n$  results in  $\chi$  being a continuous, multivalued function. In order to restrict the area of interest to a small region of  $(\xi, \zeta)$  space in the immediate vicinity of the origin so that the two complex wave functions described in equation 1.4,  $\beta_e$  is kept small.

Let us now reduce the angle  $2\alpha$  that separates the normals of the two wavefronts to zero, moving the dislocations apart and allowing the study of the structure of a single dislocation without the distortion caused by the neighboring dislocations in the row. Let us now define the constants  $A_0$  and  $\beta_e^*$  such that

$$\begin{aligned} A_0 &= 2a_0 \sin\alpha \\ \beta_e^* &= \beta_e \cot\alpha \end{aligned} \quad (1.10)$$

We can now express  $\rho_2$  and  $\chi$  in terms of these new constants:

$$\begin{aligned} \rho^2 &= A_0^2(k^2x^2 + \beta_e^{*2}(kz - \omega t)^2) \\ \chi &= \arctan\frac{\beta_e^*(kz - \omega t)}{kx} + kz - \omega t + 2n\pi \end{aligned} \quad (1.11)$$

Equation 1.11 describes a single edge dislocation parallel to the axis  $O_y$ , passing through the origin  $O$  at  $t = 0$  before moving parallel to  $O_z$  at a speed  $\omega/c$ . The constant  $\beta_e^*$  as defined above is a measure of the monochromaticity of the pulse, with a value of  $\beta_e^* = 0$  results in a dislocation that is infinitely extended along the  $O_z$  axis.

### Screw and mixed edge-screw dislocations

Consider two monochromatic waves A and B, oriented at a non-zero angle to one another. These waves are modulated linearly along a common axis in such a way that as a crest on one wave rises, the corresponding crest on the other wave falls. The effect of this interference can be seen in figure ??<sup>5</sup>, and that is that, for identical amplitudes in the plane  $y = 0$ , if the amplitude of one wave dominates above this plane and the amplitude of the other dominates below, then on the plane itself there will exist a set of screw dislocations parallel to  $O_z$  and of equal spacing along  $O_x$ . One can also achieve mixed screw-edge dislocations by simply adding modulation along the direction of propagation. If, however,  $\beta_e^* = 1$ , then the dislocation will shrink to a point, and the inverse tangent in equation 1.11 is the polar coordinate angle  $\theta$  as measured from the x-axis. Thus we have, for  $\beta_e^* = 1$ ,

$$\begin{aligned} \text{grad}\chi &= \text{grad}\theta + k\mathbf{n}_z \\ &= \mathbf{n}_\theta/r + k\mathbf{n}_z \end{aligned} \quad (1.12)$$

---

<sup>5</sup>Figure attributed to *Dislocations in Wave Trains*, 1974, doi: 10.1098/rspa.1974.0012

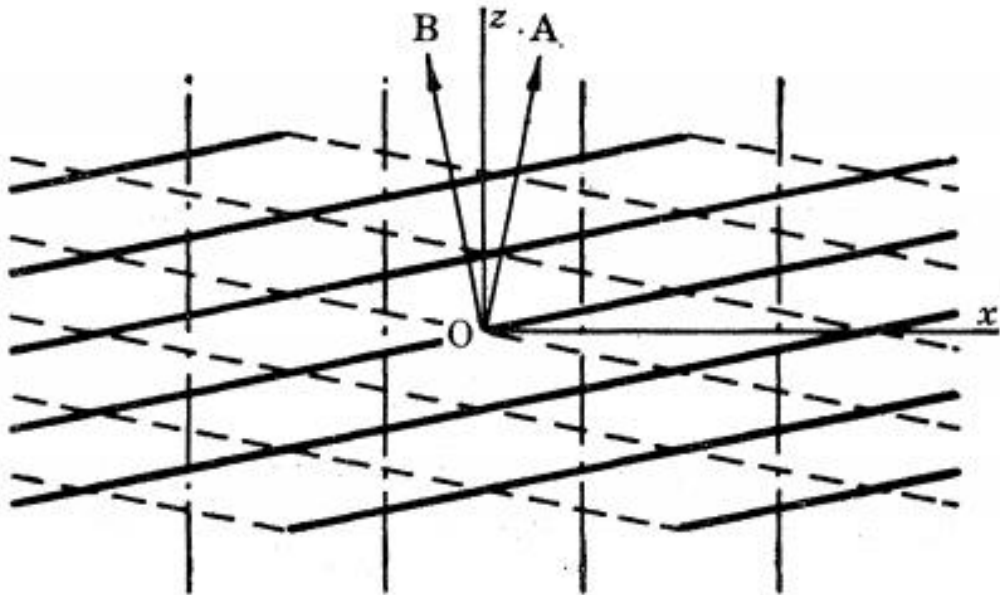


Figure 1.4: Two monochromatic plane waves, A and B traveling at different orientations to the x-axis, interfere at an angle to one another. This results in a set of parallel screw dislocations in a plane parallel to the  $O_z$  axis.

where  $\mathbf{n}_\theta$  and  $\mathbf{n}_z$  are unit vectors. This leads to the conclusion that  $\text{grad}\chi$  is the sum of the uniform field along the z-axis and is thus a vortex. The dislocation can generally be thought of as a vortex that is being carried along by the wave in the same sense that a water vortex is carried along by the flow of water, and when  $\beta_e^* \neq 1$  then the vortex can be considered to be distorted. The analysis of edge, screw, and mixed edge-screw dislocations is all done as a part of the one process. Let us define the

wave A and B describes above as

$$\begin{aligned}\psi_A &= a_0(1 - \beta_e(k_1x + k_3z - \omega t) + \beta_s k_1 y) \dots \\ &\quad \exp(i(k_1x + k_3z - \omega t - \frac{1}{2}\pi)) \\ \psi_B &= a_0(1 + \beta_e(-k_1x + k_3z - \omega t) - \beta_s k_1 y) \dots \\ &\quad \exp(i(-k_1x + k_3z - \omega t + \frac{1}{2}\pi))\end{aligned}\tag{1.13}$$

The interference pattern produced by these two waves,  $\psi = \psi_A + \psi_B$ , leads to

$$\psi = 2a_0((1 - \beta_e\xi)\sin\xi + i(\beta_e\zeta - \beta_s\eta)\cos\xi)\exp(i\zeta) = \rho\exp(i\chi)\tag{1.14}$$

where  $\rho$ ,  $\chi$ ,  $\xi$ ,  $\eta$  and  $\zeta$  are defined as in the previous section. It can then be deduced from 1.14 that

$$\rho^2 = 4a_0^2((1 - \beta\zeta)^2\sin^2\zeta + (\beta_e\zeta - \beta\xi)^2\cos^2\xi)\tag{1.15}$$

where  $\rho \geq 0$ , and

$$\chi = \arctan\left(\frac{\beta_e\zeta - \beta_s\eta}{(1 - \beta_e\xi)\tan\xi}\right) + \zeta + 2n\pi\tag{1.16}$$

From equation 1.14 we can deduce that the dislocations are described by the equations

$$\begin{aligned}\xi &= m\pi \\ \beta_e\zeta - \beta_s y &= 0\end{aligned}\tag{1.17}$$

which are derived by setting  $\psi_c = \psi_s = 0$ . Additionally, one can set  $t = 0$  and derive

$$\beta_e^* z - \beta_y = 0\tag{1.18}$$

while ignoring the solution  $\beta_e \zeta = 1$  as it lies outwith the field of interest.

We now proceed to define the constants  $\beta$  and  $\delta$  in such a was so that

$$\begin{aligned}\beta_e^* &\equiv \beta \cos \delta \\ \beta_s &\equiv \beta \sin \delta\end{aligned}\quad (1.19)$$

We can now define  $\delta$  to be the inclination of the dislocation lines to the axis  $O_y$ . We can now define the parameters that define the dislocations as follows:  $\delta = 0$  corresponds to  $\beta_s = 0$  and subsequently to pure edge dislocations. A value of  $\delta = \frac{1}{2}\pi$  corresponds to  $\beta_e^* = \beta_e = 0$  and pure screw dislocations.

If we let  $\alpha \rightarrow 0$  then

$$\begin{aligned}\rho^2 &= A_0^2(k^2x^2 + (\beta_e^*(kz - \omega t) - \beta_s k y)^2) \\ \chi &= \arctan \frac{\beta_e^*(kz - \omega t) - \beta_s k y}{kx} = kz - \omega t + 2n\pi\end{aligned}\quad (1.20)$$

The above equation describes a single mixed edge-screw dislocation in the  $yz$  plane at an angle  $\delta$  to  $O_y$ , passing through  $O$  at  $t = 0$  and moving parallel to  $O_z$  at a velocity  $c$ . Obtaining from this expression that of a pure screw dislocation is as simple as setting  $\beta_e^* = 0$ , which yeilds

$$\begin{aligned}\rho^2 &= A_0^2(k^2x^2 + \beta_s^2 k^2 y^2) \\ \chi &= -\arctan \frac{\beta_s y}{x} + kz - \omega t + 2n\pi\end{aligned}\quad (1.21)$$

It can be seen from the expression for  $\chi$  that if one were to encircle the  $z$ -axis at constant  $z$  and  $t$ , that  $\chi$  will change by  $2\pi$  for each revolution. When  $\beta_s = 1$ , the surfaces of constant phase are formed into a helicoidal shape and it is quite simple to obtain the complex wave function

$$\psi = A_0 k r \exp(i(kz - \omega t - \phi)) \quad (1.22)$$

where  $r, \phi$  and  $z$  are cylindrical polar coordinates. This is one of the special cases in which a dislocation can be found to exist in a monochromatic wave, with  $\beta_e^* = 0$  being the monochromatic limit.

# CHAPTER 2

## Experimental apparatus

The equipment used for each of the three experiments detailed in the following chapters was mostly unchanged from one project to the next. Figure 2.1 illustrates the experimental setup for the polyphonic vortex experiment detailed in chapter 4. The vortices were generated using a circular speaker array housed inside an annular enclosure composed of a double-skinned wall of lead-lined acoustic insulation foam. These speakers were driven by a signal produced first by an analogue circuit on the underside of the enclosure, which was subsequently replaced with a digital sound card connected to a PC for additional functionality. The microphone has remained unchanged throughout, although it was first connected to a spectrum analyzer for recording output to a floppy disk, which was also replaced, at the same time as the drive electronics, with the instrumental input on the front of the sound card.

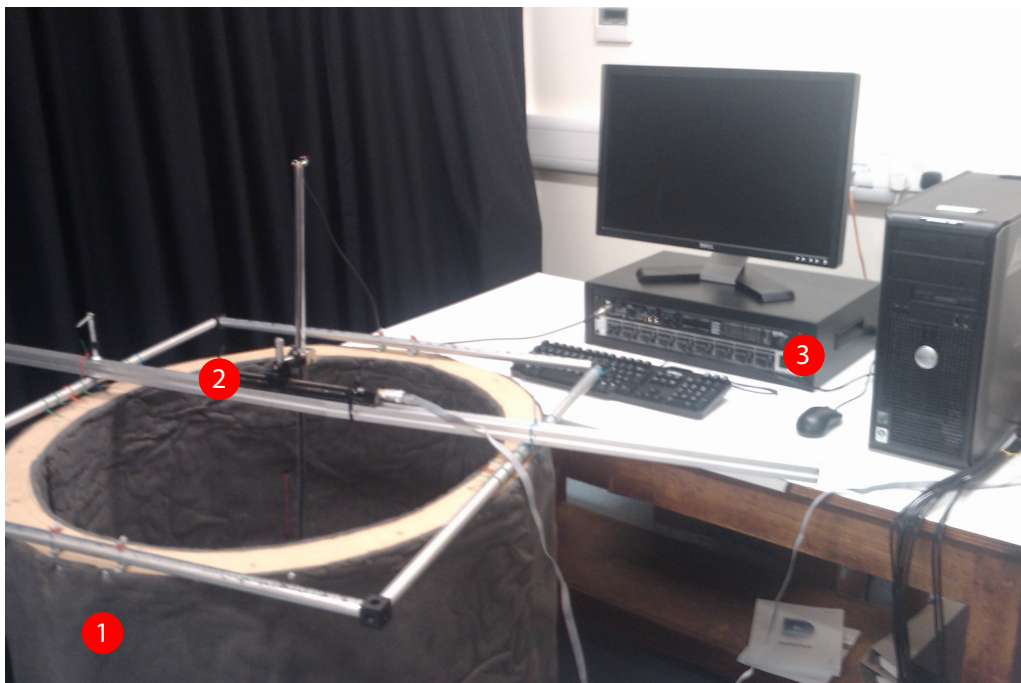


Figure 2.1: Photograph of the experimental setup for the polyphonic vortex experiment (see chapter 4). Seen in the picture is the enclosure that housed the speakers (item 1), the translation stage to which the microphone was attached (item 2) and the digital sound card and amplifier deck (item 3). Item 1, in its current form, has been a part of the setup from the beginning. Item 2 was originally a styrofoam disk suspended from a mount high above the experiment, which was used for the acoustic spanner experiment, and was then replaced with a microphone attached to the translation stage for the polyphonic vortex and phase profile experiments. Item 3, the digital sound card and amplifier deck, was added to the setup in order to replace the analogue circuitry that was used in the acoustic spanner experiment in chapter 3



Figure 2.2: The circular array of loudspeakers used in all three experiments, with the microphone used in the polyphonic vortex and phase profile experiments seen suspended in the centre of the array. It should be noted that despite there being sixteen speakers shown in the figure, only eight, every alternating one, was connected.

## 2.1 Generating and detecting the vortices

The core component of each experiment was the loudspeaker array used to generate the vortices. Item 1 marked on figure 2.1 refers to the vortex generator itself. This piece of apparatus consisted of an array of loudspeakers arranged in a circle at the bottom of a double-skinned enclosure of lead-lined foam. The eight loudspeakers at the bottom of this enclosure are 0.08m in diameter and have an impedance of  $8\Omega$ , and are arranged in a ring approximately 0.9m in diameter.

This arrangement is illustrated in figure 2.2. It should be noted that

although sixteen speakers can be seen in figure 2.2, only eight of them are attached to the sound card and being used in the experiments. The foam enclosure itself was constructed in an attempt to minimize interference from the surrounding laboratory environment. For the frame, eight posts, each approximately 1m long, were attached vertically around the edge of the base and secured at the top with an annulus with a width of approximately 0.05m between its internal and external circumferences, and whose diameter at its outer edge was equal to that of the base. This frame was then wrapped, both internally and externally, with sheets of acoustic insulation foam lined with very thin sheets of lead. This obviously does not result in a perfect  $\ell = 1$  vortex, rather an approximation to one which, in the context of our experiments was sufficient.

Item 2 in figure 2.1 is the translation stage that was used to traverse the microphone across the vortex which can be seen more clearly in figure 2.3. This stage was used in both the polyphonic vortex experiment described in chapter 4 and the high-order phase profile experiment described in chapter 5. During the experiment however, the length of the stage limited the taking of measurements to approximately 0.1m on either side of the zero position.

Item 3 on figure 2.1 is the rack in which are mounted the Motu 828mkIII digital sound card and an eight channel amplifier deck. The eight analogue output channels of the sound card were connected to the corresponding input channels on the amplifier deck. The output channels of the amplifiers were subsequently connected to each of the speakers

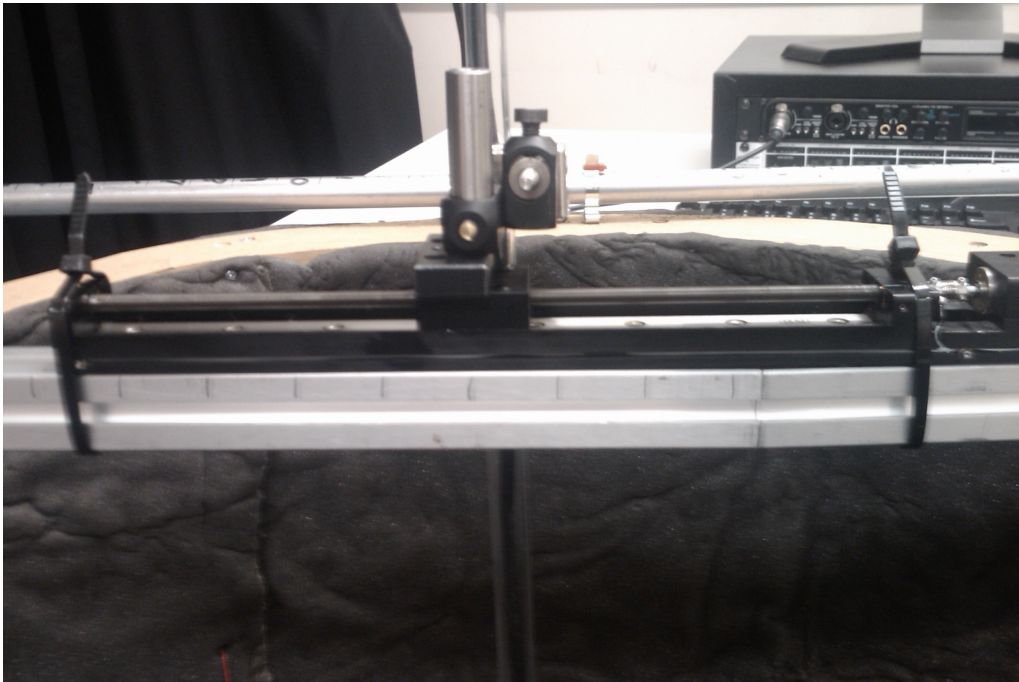


Figure 2.3: Translation stage with attached microphone. The microphone was held stationary for the quantum core experiment, and the stage was added later in order to take 2-dimensional scans of the polyphonic vortex.

on the vortex generator. The sound card is also connected to the PC via a Firewire 800 connection which allows it to receive a signal produced using Labview. There is also a connection between the microphone and one of the instrumental connections on the front of the sound card allowing feedback from the microphone to be acquired and processed by the sound card.

A complete view of the vortex generator can be seen in figure 2.4. The square frame seen secured to the top of the housing was used to acquire the 3D amplitude graph seen in figure 4.2. To do this, a number of marks were placed along parallel sides of the frame and these were used to align the post to which the translation stage was attached. The

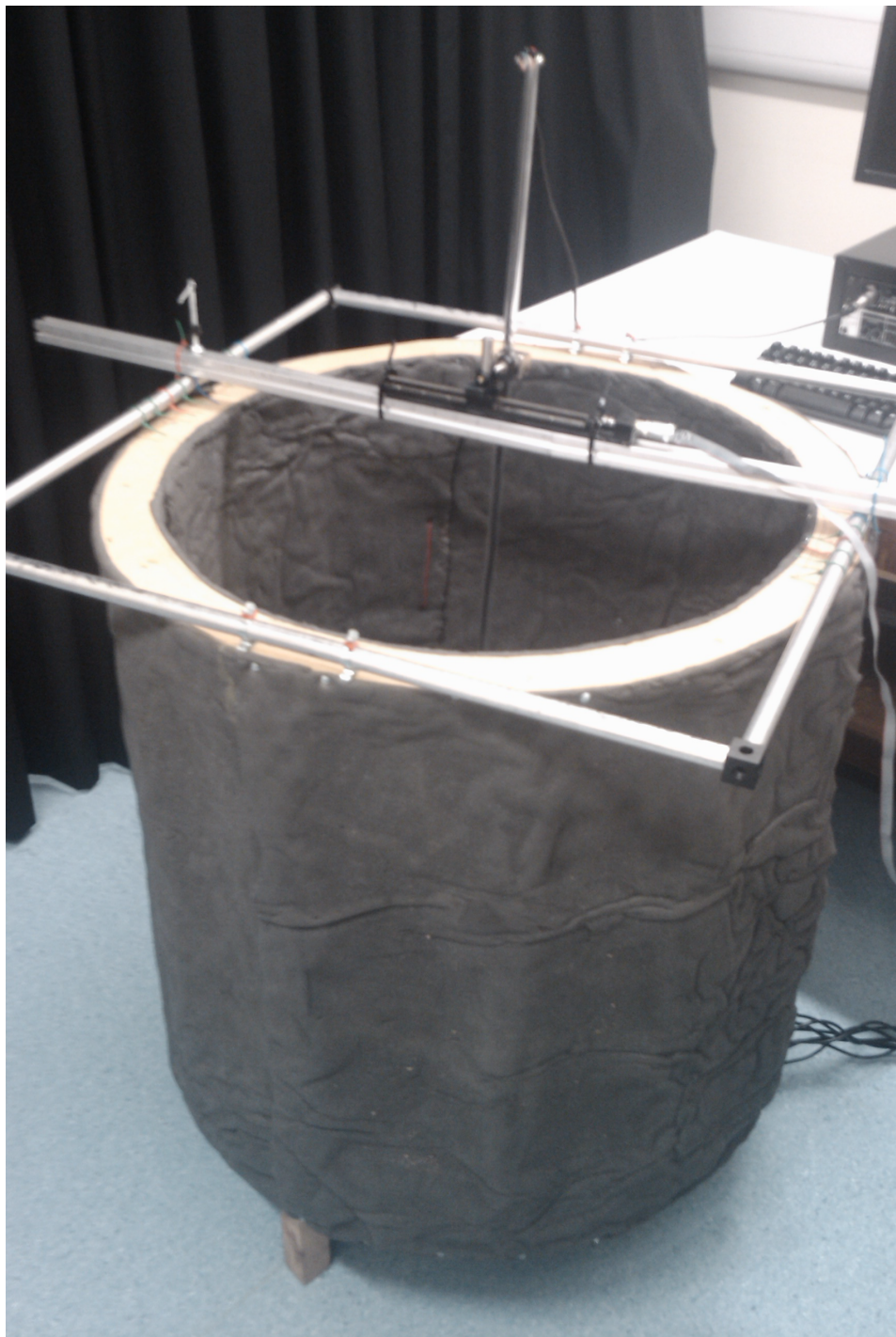


Figure 2.4: The enclosure containing the speaker array. The grey material on the interior and exterior walls is lead lined foam that was applied in order to increase the acoustic insulation.



Figure 2.5: A styrofoam disk suspended above the speaker array. The grey objects are weights that were applied in order to balance the disk. A schematic of this arrangement may be seen in figure 2.6

grey material seen coating the interior and exterior of the enclosure is lead-lined acoustic insulation foam. This was applied in an attempt to reduce the effect of interference from the surrounding laboratory environment and to prevent drafts of air from disturbing the styrofoam disc that was suspended inside the enclosure for the acoustic spanner experiment.

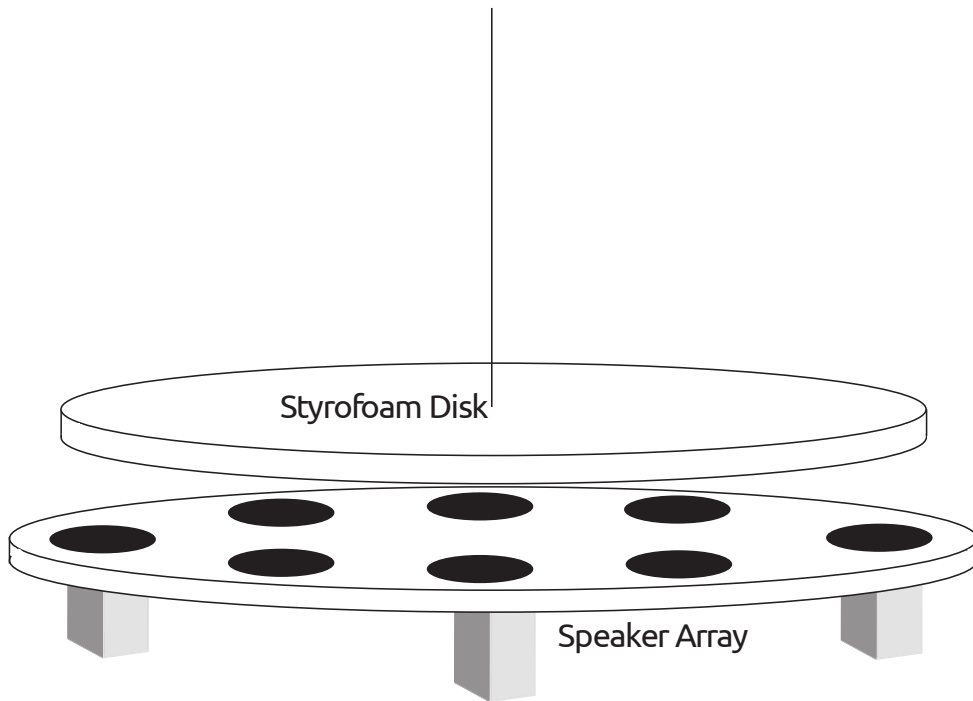


Figure 2.6: A styrofoam disk suspended above the speaker array. A physical example of this may be seen in figure 2.5.

## 2.2 Acoustic spanner

Figure 2.5 shows the styrofoam disk used to demonstrate the acoustic spanner in chapter 3. The disk consisted of two identically sized foam disks, stuck together top to bottom so as to produce a single double thickness disk. The diameter of the disk was approximately 0.8m. A hole was then drilled through the centre of the disk and a length of wire was threaded through it before being secured. The opposite end of the wire was then secured high above the enclosure leaving the disk hanging freely. The disk was suspended approximately 0.06m above the speakers, allowing it to interact with the sound waves before they had a chance to disperse. Lengths of wire of various diametres were used during the

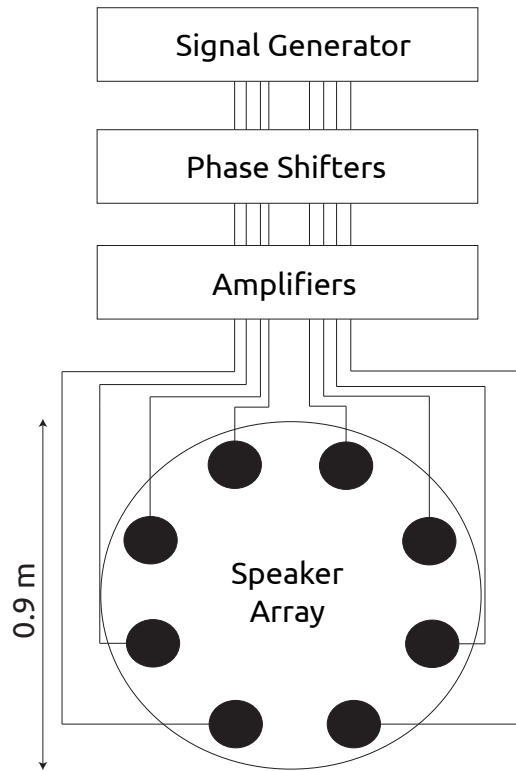


Figure 2.7: An illustration of the acoustic spanner experiment.

acoustic spanner experiment, notably  $50$  and  $60\mu m$ . The two dark shapes seen on opposite edges of the disks in figure 2.5 are additional pieces of (denser) foam that were attached to the disk to act as a balancing mechanism, since the hole wasn't drilled precisely in the centre of the disk. An illustration of the experimental setup for the acoustic spanner experiment can be seen in figure 2.6, with the disk suspended by thin wire above the speaker array.

In order to rotate the styrofoam disk and demonstrate the acoustic spanner, a monophonic acoustic vortex had to first be generated. Figure 2.7 illustrates the basic setup for the process. Throughout the entire

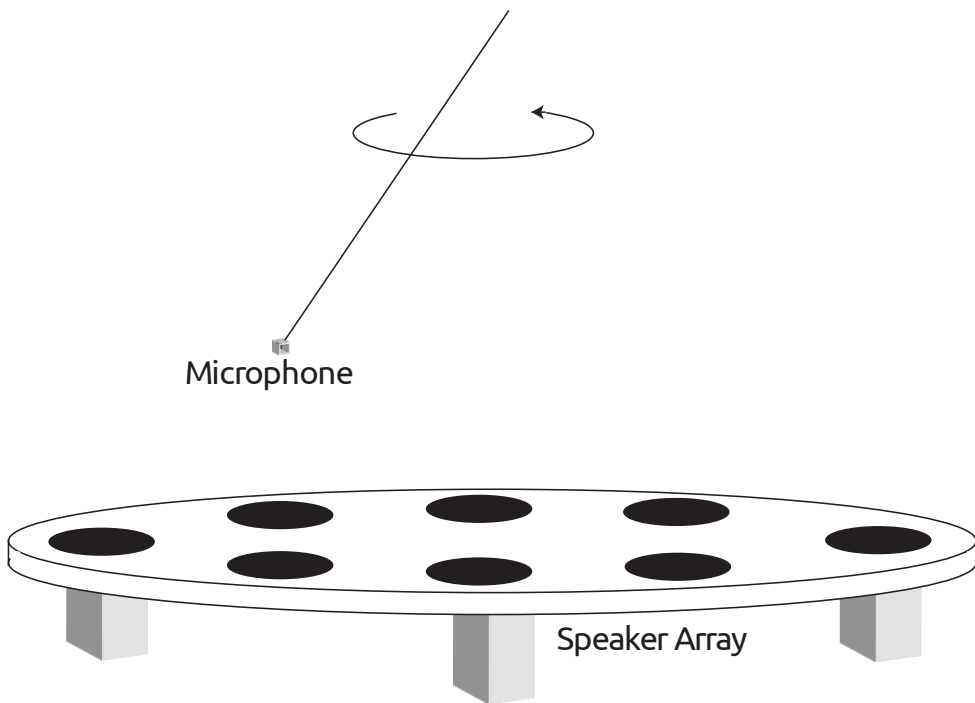


Figure 2.8: An illustration of the measurement of the rotational Doppler shift of the acoustic spanner,

experiment the vortex was generated using analogue electronics. First, a 500Hz signal was generated using an external signal generator and a 12V power supply. This signal was sent to a series of low-pass filters in order to impart a phase delay before finally being driven to the amplifiers and onto the speakers. In order to reverse the direction of the vortex, the direction of the phase delay was simply reversed by swapping opposing phase values with one another. This was initially achieved using a set of mechanical switches attached to the side of the speaker array, but in order to reduce the effect of outside interference of the system, these were removed and replaced with a single switch on the end of a length of wire so as to decouple the switching mechanism from the experiment

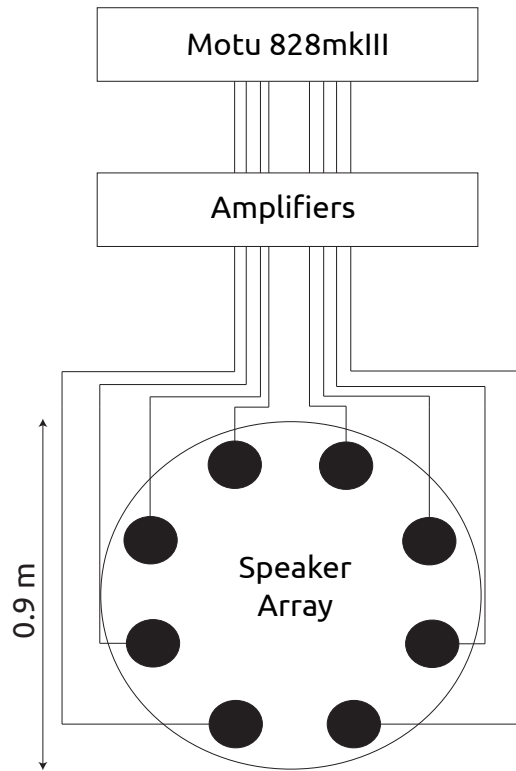


Figure 2.9: An illustration of the polyphonic vortex experiment.

and thus eliminate the need for anyone to be around the experiment during the measurement process.

## Doppler shift

The rotational Doppler shift of a radiation source is measured by rotating the source with respect to the detector. Given the size of the vortex generator, this method would be impractical, so it was decided to simply rotated the detector, the microphone in this case, with respect to the speakers. The microphone was inserted into the end of a hollow plastic tube, whose internal diameter was almost exactly the same

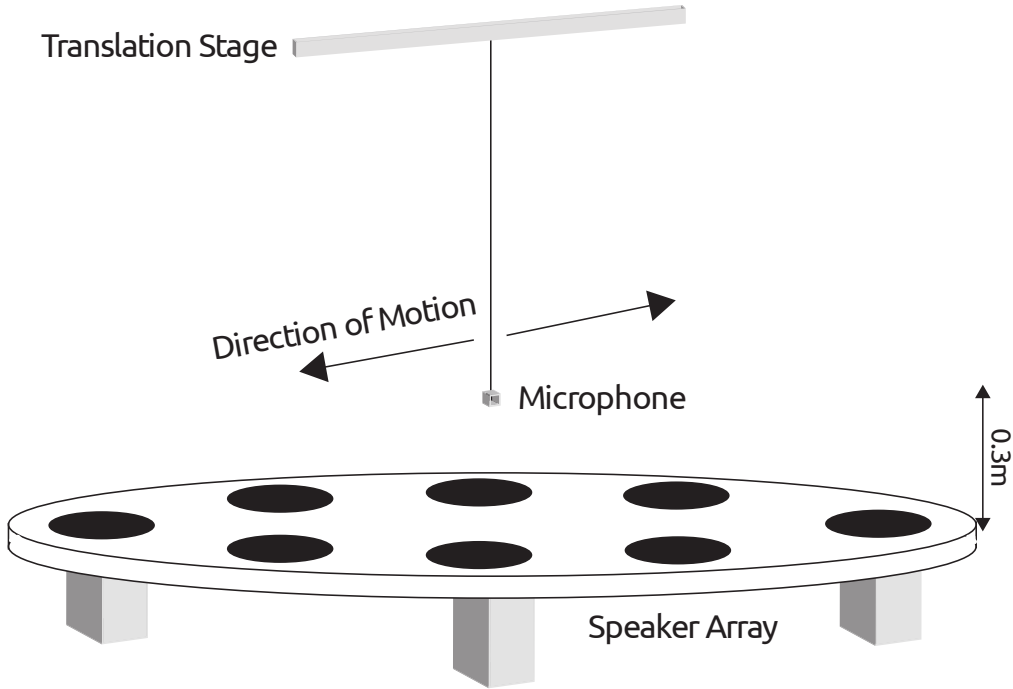


Figure 2.10: An illustration of the measurement of the polyphonic acoustic vortex.

diameter of the microphone, and the cable connecting the microphone to the instrumentation was run up the centre of the rod. During the measurement process, the rod was rotated by hand around the inside edge of the enclosure, resulting in, from the perspective of the measurement apparatus, a drag on the frequency of the vortex.

## 2.3 Polyphonic vortex

Although the analogue circuitry was sufficient for the investigation of the acoustic spanner using a monophonic acoustic vortex, using such a setup to generate a polyphonic vortex proved very problematic, due to the complexity of the electronic circuitry that would be required, so it was



Figure 2.11: Motu 828mkIII digital sound card.

decided to replace the analogue electronics with a more sophisticated set of equipment. Given the complexity of the signal we were attempting to generate, it was decided that using a computer running Labview would be the easiest solution for generating the desired signal. This signal was subsequently output, using a Firewire 800 connection, to a Motu 828mkIII digital sound card, which can be seen in figure 2.11<sup>1</sup>. This device is equipped with eight analogue output channels which allowed us to address each speaker with an individual signal sent from the computer. With this card, a set of amplifiers would also be needed and so an eight channel analogue amplifier deck was also added to the setup. The sound card also came equipped with two instrumental input channels, one of which was utilized for acquiring feedback from the microphone.

---

<sup>1</sup>Figure attributed to MOTU, Inc - <http://www.motu.com/products/motuaudio/828mk3>

# CHAPTER 3

## An acoustic spanner and its associated rotational Doppler shift

### 3.1 Introduction

Neither spin nor orbital angular momentum are exclusively quantum phenomena. It is possible to calculate both quantities directly from the cross products of the EM fields, and then appropriately integrated over the beam cross-section [9]. It should also be noted that waves that carry both momentum and energy are not solely the property of electromagnetic radiation, and rather that they are a generic property of all transverse and longitudinal waves. The ratio of the cycle-averaged momentum flux  $\langle P \rangle$  to the energy flux  $\langle E \rangle$  is the reciprocal of the

phase velocity  $v_\phi$ , of the wave, i.e.

$$\frac{\langle P \rangle}{\langle E \rangle} = \frac{1}{v_\phi} \quad (3.1)$$

This expression also applies to sound waves, meaning that a 1W sound beam that travels through the air and is totally absorbed by an object, will exert a force of approximately 0.3mN. In a fluid however, sound manifests as a longitudinal wave rather than a transverse wave, and is thus described as a scalar field rather than a vector field and hence has no polarisation. This means that sound cannot carry spin angular momentum, but there is no such restriction placed on a sound wave with respect to orbital angular momentum. Indeed the linear [10] and angular [11, 12] momentum content of sound waves have been widely appreciated and compared to their optical counter parts [13, 14].

Helically phased optical beams are now typically made via the transformation of a conventional planar wave laser beam using a hologram i.e. diffractive optic [15, 16]. Rather than using holographic techniques however, acoustic vortices have been generated using various techniques including optically heated helical surfaces [17] and individually addressed transducers [12]. By analogy with the optical case, or directly [11], the ratio between the cycled-averaged acoustic angular momentum flux  $\langle L \rangle$  and acoustic energy flux  $\langle E \rangle$  is given by

$$\frac{\langle L \rangle}{\langle E \rangle} = \frac{\ell\lambda}{2\pi v_\phi} \quad (3.2)$$

Where  $v_{phi}$  is the phase velocity of the sound in the medium (approximately  $340\text{ms}^{-1}$  in air at room temperature). As a result, when

an object absorbs a helically phase sound wave, that object should be set into rotation: an acoustic spanner. It should be pointed out that during the preparation of the original paper on which this chapter is based [7], we were alerted to a similar acoustic momentum transfer experiment [18]. It was our belief that both experiments are consistent with an interpretation of our results in terms of acoustic angular momentum calculated by equation (2).

Another hallmark of helical phase beams, beyond their transfer to matter, is that they are subject to a rotational frequency shift [19]. This shift is an analogous yet distinct phenomenon to the more widely known linear Doppler shift. Whereas the linear shift is proportional to the velocity between source and observer, the rotational shift is proportional to the product of the angular momentum of the beam and the rotational velocity between source and observer. As early as 1934 [20] a frequency shift associated with the circular polarisation (spin angular momentum) was noted. More recently, it has been observed to be proportional to the sum of the spin and orbital angular momentum of a beam of light [21]. A sound wave of angular frequency  $\omega_s$  would therefore undergo a frequency shift of

$$\Delta\omega_s = \ell\omega_r, \quad (3.3)$$

where  $\omega_r$  is the relative angular velocity between the source and observer.

## 3.2 Generating helically phased acoustic beams

The experimental apparatus used to generate the helical phase acoustic beams can be seen in chapter 2. A circular array of loudspeakers was assembled comprising eight speakers in a circle of approximately 0.52m across, with each individual amplifier capable of providing up to 10W of electrical power. The loudspeaker array was itself mounted into the base of a 0.7m diameter cylinder constructed from sound absorbing lead-foam laminate. This laminate absorbs over 90% of the incident sound energy.

The signal delivered to these speakers was generated using a signal-generator feeding into a phase-shifter circuit providing eight outputs with sequential ( $\pi/4$ ) steps. The orientation of these steps (either increasing or decreasing) could be controlled with a simple logic switch, allowing the direction of rotation of the spanner to be altered. The outputs from the phase shifter circuit are individually amplified to produce a final set of signals of approximately equal amplitude which are fed to the loudspeakers.

The resulting acoustic beam that is emitted by the loudspeakers is anticipated to possess a helical phase structure described by  $\exp(i\ell\phi)$ , where  $\ell = \pm 1$  (phase change per axial revolution of the acoustic beam of  $\pm 2\pi$ ) depending on the setting of the logic control. The speakers were driven with a frequency of around 500Hz, corresponding to an acoustic wavelength of 0.68cm.

### **3.3 Acoustic spanner**

Given the design of the apparatus, one might expect the acoustic beam to diverge as it propagates, with each speaker acting as a point source and with the walls of the enclosure affecting the propagation field in some way. This could be assumed to result from the acoustic wavelength being of the order of the diameter of the speaker array, however due to the interference of the eight signals, a helically phased beam with a minimum intensity along the beam axis is established. This beam is directed upwards toward a 0.6m diameter styrofoam tile, constructed from sheets of acoustic insulation foam, and suspended from a length of steel wire above the speaker array. The sound field in the near-field, i.e. approximately 0.15m from the speakers, has an annular intensity profile which is suggestive of a Laguerre-Gaussian mode. Positioning the disk at this distance allowed for the most efficient transfer of momentum from the wavefront to the disk. Upon closer examination, it was found that this profile was just an approximation to L-G, however this had no effect on the final outcome as the orbital angular momentum to energy ratio is simply a function of the helical phase fronts and as such is unchanged between the near and far fields. Figure 3.2 show the results of multiple measurements taken of the beam. A cross-section of the beam was probed using the microphone and the results indicate that the sound field is remarkably consistent.

In order to isolate the experiment and reduce the effect of interference from the laboratory environment, the observations were

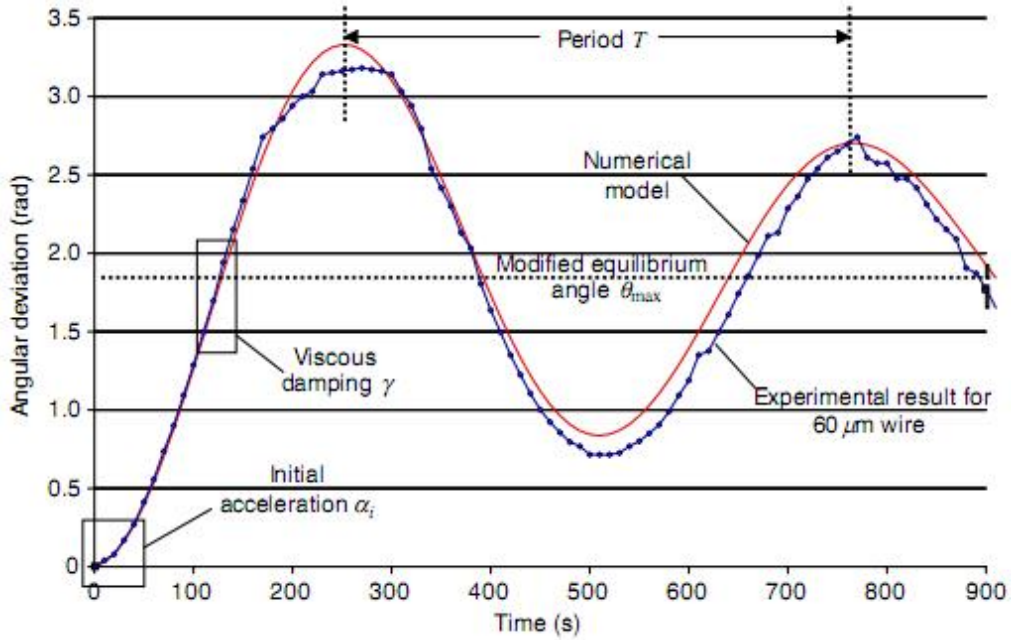


Figure 3.1: Comparison of the motion of the pendulum calculated from the equation of motion and the observed angular displacement. The parameters for damping and stiffness constant are deduced from observation and the resulting agreement between predicted and observed motion is good. Measurements of torque can be deduced from  $\alpha_i$  ( $\Gamma_s = I\alpha_i$ ) or  $T$  and  $\theta_{max}$  ( $\Gamma_s = 4\pi I\theta_{max}/T^2$ ).

carried out using a video camera positioned above the disk and pointing downward, with the output being fed to a remote monitor over which was laid an angular scale. In order to establish a reproducible set of observations, we made measurements with various suspension wire radii and lengths. The logic control of the phase shifter circuit was used to remotely change the angular momentum direction while recording results.

Starting with the tile initially at rest, the sound field was switched on and the resulting angular motion observed. The differential equation

governing the motion of the torsional pendulum is

$$\Gamma_s = I\ddot{\theta} + \gamma\dot{\theta} + k\theta \quad (3.4)$$

where  $\theta$  is the angular displacement,  $\Gamma_s$  is the torque exerted on the tile by the incident acoustic beam,  $I$  is the moment of inertia of the tile (0.022 kgm<sup>2</sup>),  $\gamma$  is the viscous damping coefficient and  $k$  is the torsional stiffness constant of the pendulum. The motion is that of an under-damped torsional pendulum.

The various parameter shown in figure 3.1 could all be deduced from observations of the motion of the disk, and the plot in the figure shows the results of an experimental measurement of the motion compared to that predicted by equation 3.4. Using the initial acceleration  $\alpha_i$ , the period of oscillation  $T$  and the final rest angle  $\Theta_{max}$ , one can deduce  $\Gamma_s$  can be calculated thus:

$$\Gamma_s = I\alpha_i \quad (3.5)$$

Also, if one were to consider the pendulum to be undergoing simple harmonic motion with period  $T = 2\pi\sqrt{\frac{1}{k}}$ , the torsional stiffness constant  $k$  may be deduced. Thereafter, we can use this value for  $k$  along with  $\Theta_{max}$  to give

$$\Gamma_s = k\theta_{max} = \frac{4\pi^2 I}{T^2}\theta_{max} \quad (3.6)$$

Finally, these values for torque can be compared with an estimation of the acoustic torque based on the acoustic power incident on the tile. Lengths of steel wire of radii 50 and 60  $\mu m$  respectively were used in the experiment. The measurements recorded for these radii can be seen in table ?? were the torsional displacement for different parameters, as

| $r(\mu\text{m})$ | $L(\text{m})$ | $\theta(\text{rad})$ | $\Gamma(\text{Nm}) (\alpha_i)$ | $\Gamma(\text{Nm}) (\theta_{max}, T)$ |
|------------------|---------------|----------------------|--------------------------------|---------------------------------------|
| 50               | 1.89          | 5.8                  | $5.6 \pm 1.4 \times 10^{-6}$   | $6.0 \pm 0.6 \times 10^{-6}$          |
| 60               | 1.22          | 1.95                 | $4.5 \pm 1.8 \times 10^{-6}$   | $6.5 \pm 0.7 \times 10^{-6}$          |

Table 3.1: Summary of acoustic spanner results. Torque values are shown for the methods described in the text, using the initial and long-term parts of the observed motion. Ideally, for a given acoustic set-up, we would expect the torque to be independent of suspension wire radius and comparable to the value measured from the properties of the acoustic beam (estimated to be  $6.4 \times 10^{-6} \text{ Nm}$ ).

described in equations 3.4 and 3.5, are recorded. It should be noted that in the case of the  $50\mu\text{m}$  wire, the value of 5.8 radians recorded for  $\theta_{max}$  is close to one full rotation of the disk. The torque values calculated from the initial acceleration and modified equilibrium position are shown. The results shown have been averaged over  $\ell = \pm 1$  for each configuration of the suspension. It should be noted that given the uncertainties present in both the measurement and system parameters, the torque values detailed in table ?? are reasonably consistent with each other. If one were to assume that each of these were free of systematics errors, then the best estimate of  $6.1 \pm 0.8 \times 10^{-6} \text{ Nm}$  would be obtained for the measured torque, which itself is statistically compatible with the individual measurements.

This value of torque is comparable to the estimate based on the acoustic power using equation 3.2. This power is itself estimated from a measurement of the electrical power being fed into the speakers assuming an audio efficiency of 0.5%. Another measurement that was taken was the average sound pressure level at the plane of the

tile which was found to agree with the electrical measurement to within the experimental uncertainty of the overall system. Having estimated the acoustic energy, the resulting torque depends upon the absorption of the tile material, which is based on information given by the manufacturer and is estimated to be 30% for our configuration, a figure confirmed by our own reflection/transmission measurements. Using this approach acoustic torque is estimated to be  $\Gamma_s = 6.4 \times 10^{-6} \text{Nm}$ , which within the experimental errors agrees with our observations.

### 3.4 Rotational Doppler Shift

While the results of the previous section indicate that orbital angular momentum is transferable across media, it is not conclusive that this is the result of a helically phased beam described by  $\exp(i\ell\theta)$ , and that this phase structure is not compromised by reflected components from the walls of the enclosure. We verified that this was indeed the case by examining another property of helically phased beams: the rotational Doppler shift. This is a phenomenon whereby the frequency, as perceived by the observer, is attenuated by the relative motion of the observer, which in this case is demonstrated with a microphone rotating around the beam axis. This experiment can be seen depicted in chapter 2. Using a microphone held stationary at any point inside the vortex of frequency  $\omega_s$ , a measured frequency of  $\omega_s$ , adjusted for its position within the helical phase front, is recorded. This microphone is then swept in a circular motion, in a plane parallel to the speaker array, with an angular

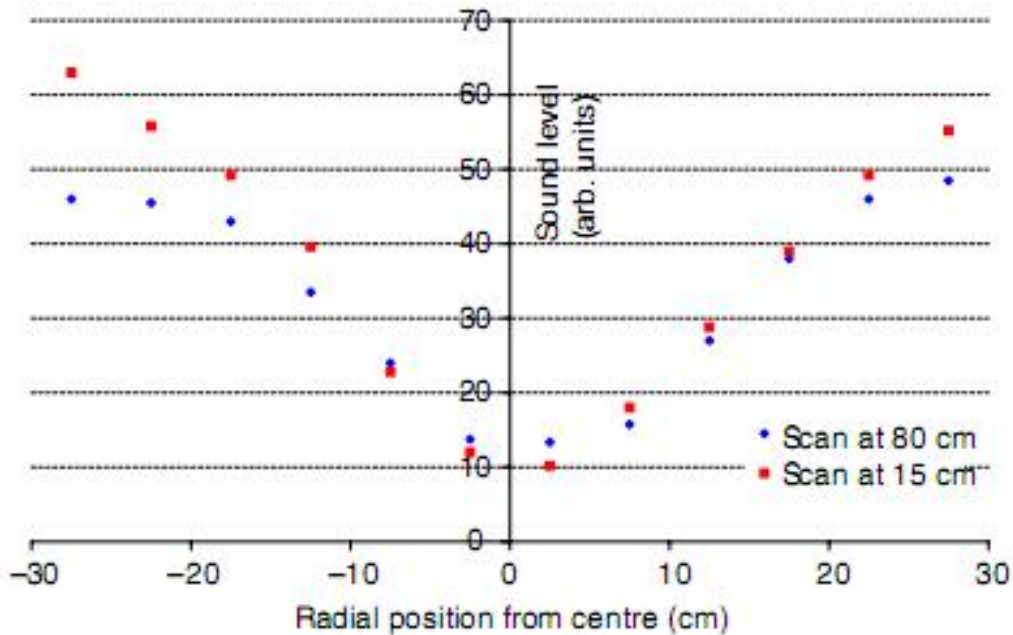


Figure 3.2: Measurements of the sound level across the diameter of the containment cylinder at the position of the acoustic tile (0.15m height above the loudspeakers) and the plane where Doppler results were taken (approximately 0.8m above the loudspeakers). Each trace represents an average of several traverse scans with a roaming microphone.

velocity of  $\omega_r$ , a rotational frequency of  $\omega_s \pm \omega_r$  is observed, where  $\omega_r$  is the value of the rotational Doppler shift, the direction of which, either upwards or downwards, is determined by the direction of rotation of the microphone. It should be noted that, in this situation, contrasts starkly with those where rotational motion results in a linear Doppler shift. This is because the distance between the source and the observer is held constant and thus no linear component of frequency shift may exist.

The rotational Doppler shift, an example of which can be seen in figure 3.3, was measured by rotating the microphone in a circular arc of radius roughly equal to that of the speaker array, and at a distance

of roughly 80cm. The signal recorded was then sent to a Stanford FFT Analyser (model SR780)<sup>1</sup>. In figure 3.2, a typical scan showing the transverse cross-section of the vortex can be seen. From this it can be seen that the sound field possess a central minimum of intensity, as would be expected for a  $\ell = 1$  helically phased beam. The dominant spectral component of the sound field clearly moves either above or below the baseline value depending on whether the microphone is rotated in the direction of increasing or decreasing phase of the helical phase front. Slight variations in the volume of successive speakers as the microphone passes around the sound field give azimuthal variation in the acoustic energy. In terms of the constituent modes this corresponds to a superposition of different ' $\ell$ ' values. As a consequence, weak sidebands are both expected and observed on either side of the shifted frequency. It should be noted that since these sidebands are both small and symmetric about the central frequency, the mean  $\ell$  value is not significantly different from  $\ell = \pm 1$ . In both cases the dominant peak occurs at the Doppler shifted frequency we would expect from equation 3.3.

---

<sup>1</sup>Device information can be found at the SRS homepage  
<http://www.thinksrs.com/products/SR780.htm>

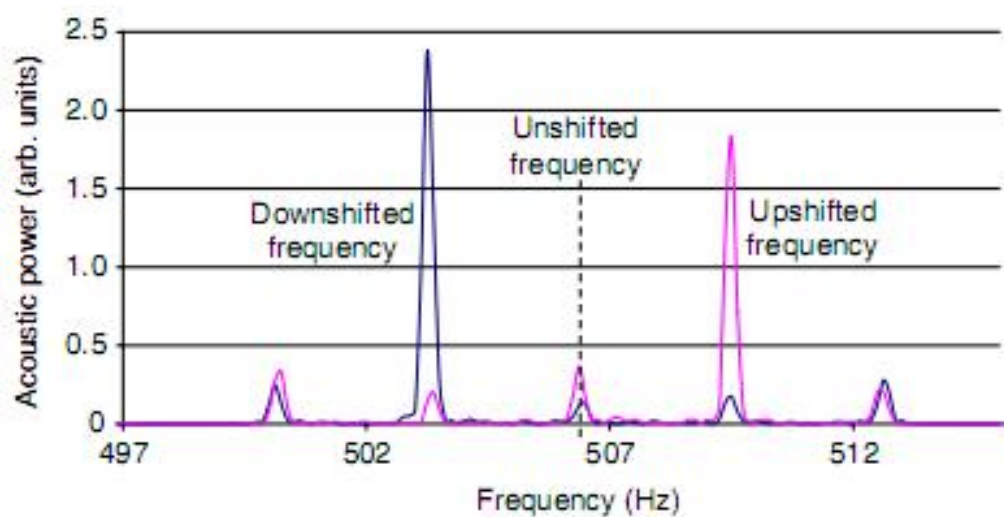


Figure 3.3: Results of the rotational Doppler effect measured with a spinning microphone. The frequency offset in Hz,  $\Delta f_z$ , is equal to the revolutions per second made by the microphone relative to the source (or  $\omega_t/2\pi$ , where  $\omega_t$  is the relative angular velocity). The downshifted frequency corresponds to the case when the microphone is rotated in the direction of increasing phase of the helical phase front.

# CHAPTER 4

## A Polyphonic Acoustic Vortex and its Complementary Chords

### 4.1 Introduction

Orbital angular momentum has been the subject of research for many years now, however the concept of an optical phase singularity has existed for much longer and has been studied in detail. These investigations were initially conducted in random or complex fields [3], and it was only later that the helical phase fronts of light beams were considered [22, 23]. It has been demonstrated that phase singularities arise whenever three or more non-collinear plane waves interfere [24, 25], and it is for this reason that they occur in all natural light fields. A typical case of this phenomena is laser speckle, where a tangle of vortex lines are mapped out by phase singularities and percolate through all space [26]. Generally the singularities of each spectral component

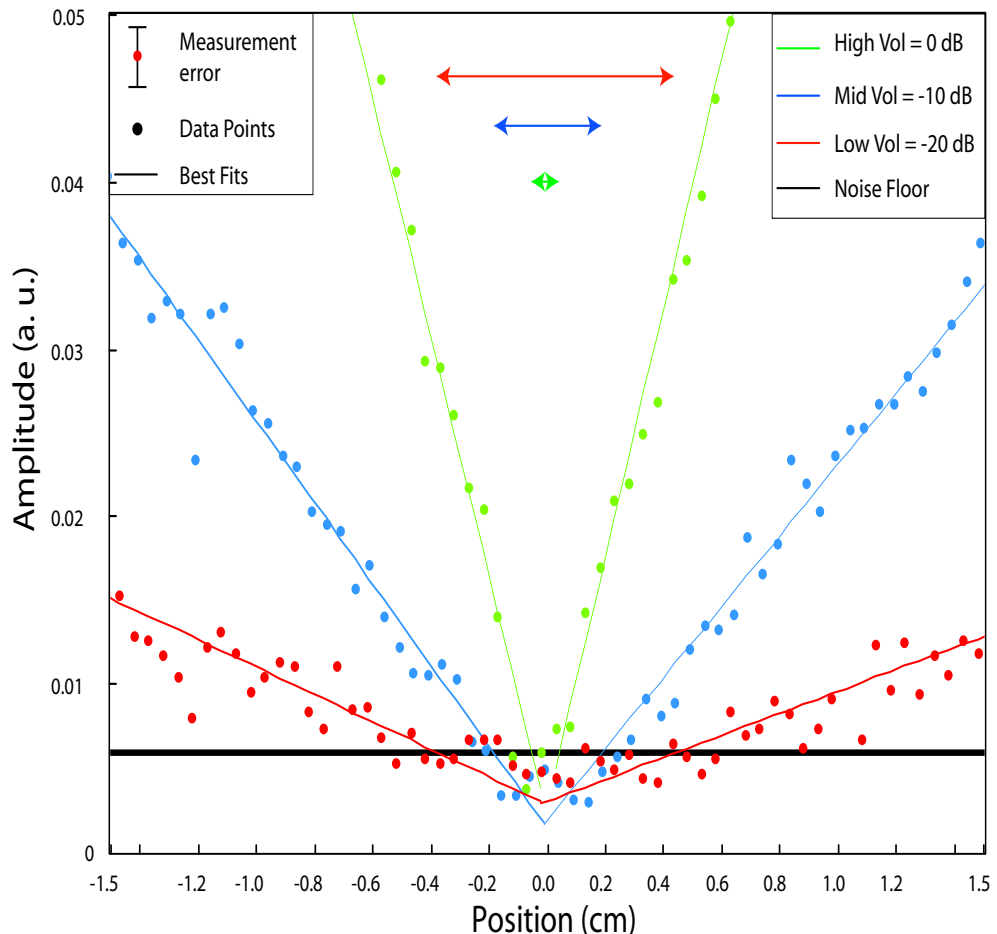


Figure 4.1: Amplitude cross-section through the acoustic vortex at 523 Hz, recorded for three different sound volumes. The points are the experimentally recorded data and the solid lines are linear best fits (not constrained to pass through zero), and the horizontal arrows mark the extent over which the noise of the measurement system dominates over the measured signal.

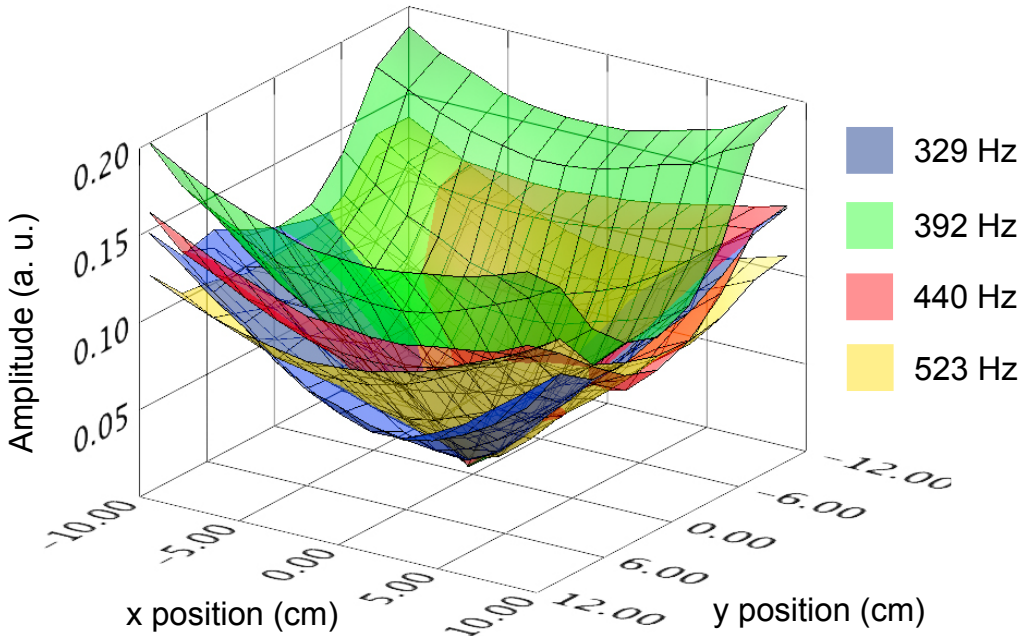


Figure 4.2: 2D plots of amplitudes corresponding to the four frequency components of the polyphonic acoustic vortex. Note that the singularities all overlap in the centre of the beam.

of these speckles do not overlap and therefore this phenomena goes unnoticed in everyday situations.

Although it is usually practical to harness only monochromatic light for experimental use, it is entirely possible to generate white light vortices in special cases, that is vortices which contain multiple temporally coherent spectral components whose singularities all overlap, resulting in a single black vortex line along the beam axis [27, 28, 29, 30]. These different spectral components can be moved apart by the perturbation of their beams resulting in a situation where each wavelength has its own discreet singularity within the transverse cross-section. It is then possible to move a camera or other imaging

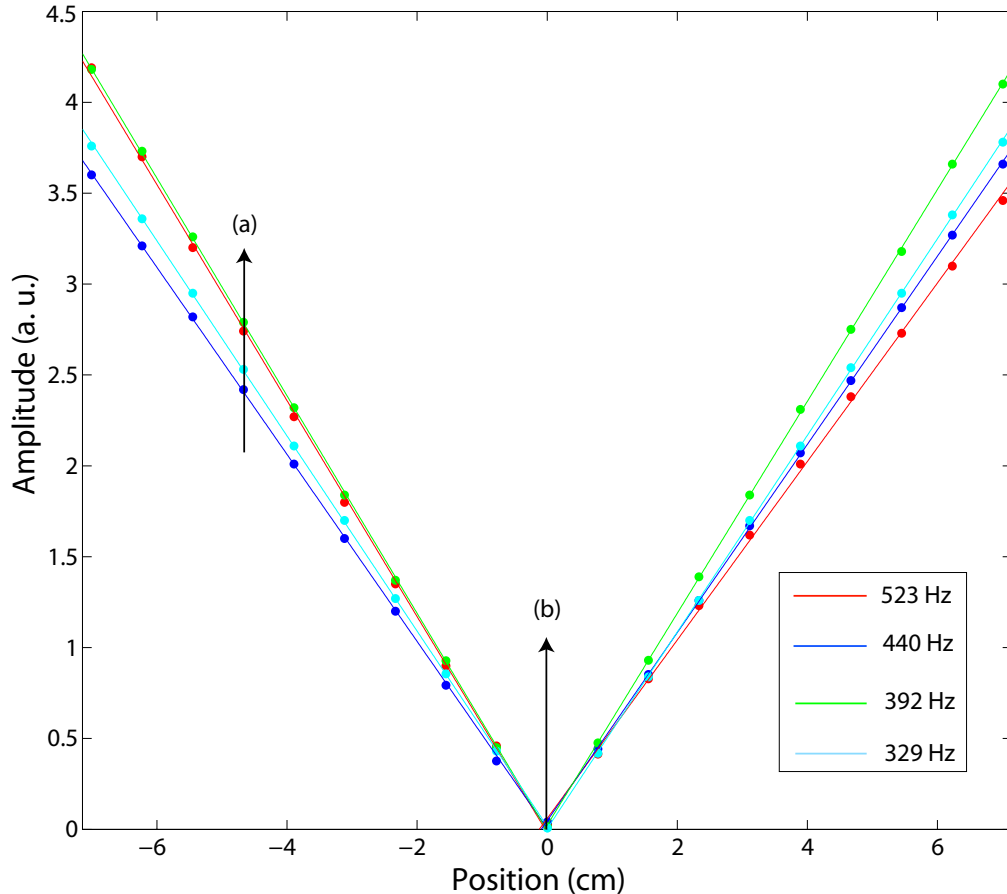


Figure 4.3: Amplitude cross-section of the polyphonic vortex recorded at much higher volume than shown in figure. 4.1. The points show the experimental data and the solid line shows the best linear fit. (a) and (b) indicate the off and on-axis positions for which the full spectral signals are shown in figures 4.4 and 4.5.

device over these singularities and detect the presence of the other wavelengths, giving a characteristic spatial spreading of complementary colours [27, 31, 32, 33, 34].

It has been shown recently that these helically phased acoustic beams are capable of setting objects into motion by imparting to them their orbital angular momentum [18, 7].

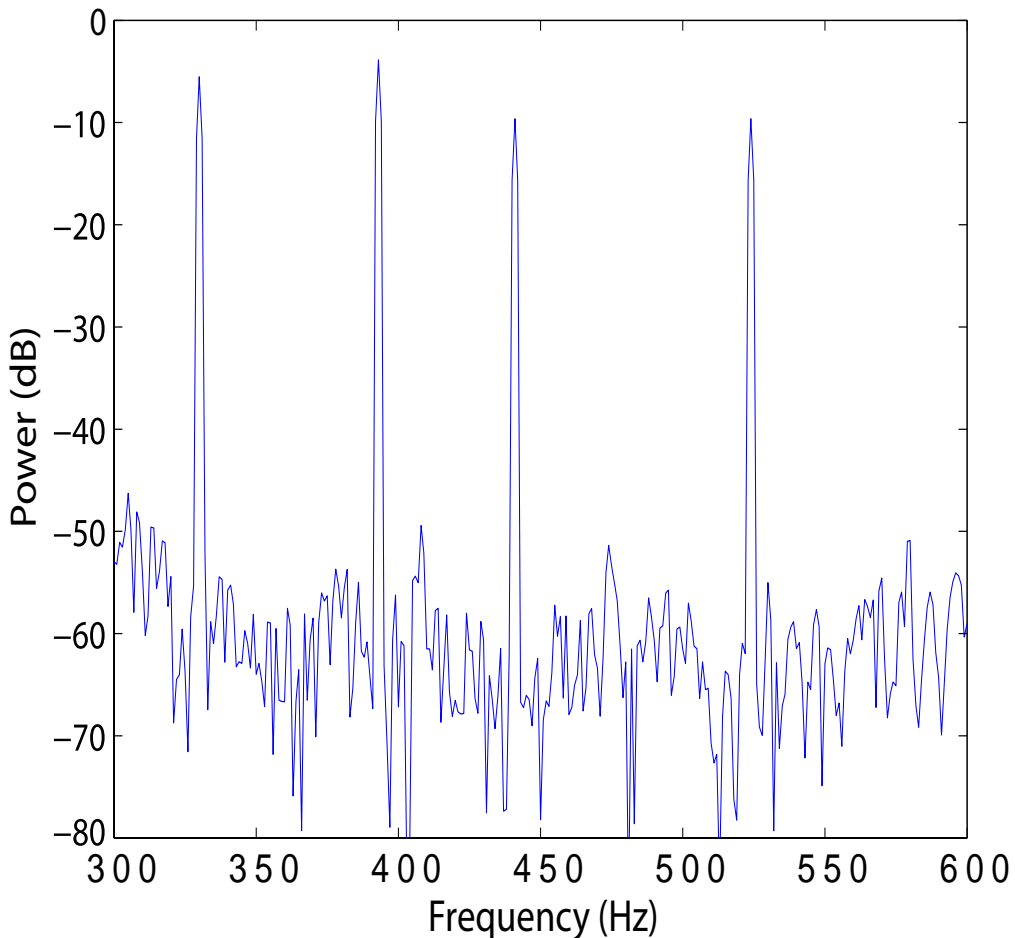


Figure 4.4: Spectral plots of the microphone signal recorded at the off (a) axis positions of figure 4.3.

The phenomena of phase singularities, vortices and orbital angular momentum are not just limited to light, but may be found within all types of wavefield. The work presented in this chapter is based on a paper published by the author [8] demonstrating this idea with the production of a polyphonic acoustic vortex and its subsequent perturbation, similar to the optical method described above. A circular array of loudspeakers was assembled so as to generate an approximation to an  $\ell = 1$  vortex

with a phase singularity in the centre. Software control of these speakers allowed us to address each speaker with an arbitrary mix of acoustic frequencies, in our case corresponding to four different musical notes. By setting the complex amplitude of each speaker, we could create a polyphonic acoustic vortex, with suppression of the sound intensity at a singularity of 45 dB. For a low-intensity beam, this suppression is sufficient to observe the noise floor of the measurement system in the centre of the vortex beam. Subsequent perturbation of the amplitudes driving the individual speakers split the vortex and created separate singularity positions for each acoustic frequency. At each of these positions one of the notes was canceled, leaving the remaining three notes to form a tri-note chord.

## 4.2 Apparatus

The acoustic vortex generated in this experiment was not a perfect  $\ell = 1$  vortex, but rather an approximation to one. This was achieved by arraying eight 0.08m diameter loudspeakers, with an impedance of  $8\Omega$ , in a ring 0.9m across (see figure 2.2). In order to minimize outside interference from the laboratory environment, the speaker array was mounted within a cylindrical enclosure consisting of a double layer of lead lined foam. An array of eight amplifiers (each rated at  $\pm 15V$ ) was used to drive the speakers with eight time synced independent wavetrains from an eight channel digital sound card (Motu 828mk3 firewire audio interface). The microphone (Knowles Electronics FG-23329-P07) can be seen in figure ??

suspended from a motorized translation stage. With this arrangement, intensity cross-sections of the sound field could be readily obtained by traversing the microphone across the diameter of the speaker array at a distance of approximately 0.3m above the speakers. Although the microphone design is not well calibrated to measure absolute sound levels, its compact size (5mm) and nominal sensitivity –53dB (volt/0.1Pa) made it ideal for sensitive measurements without unduly perturbing the sound field. Using a low noise amplifier (Laser Components (UK) Ltd, model: DLPVA-100-B-S) the output from the microphone was fed to the sound card for spectral analysis. In all cases the gain of the amplifier was set to best match the dynamic range of measured voltages to the dynamic range of the data acquisition board. In addition to producing the wavetrains to drive the loudspeakers, the same computer was used to control the translation stage on which the microphone was mounted, record the microphone output and analyse its frequency spectrum.

In order to achieve and maintain an equilibrium between the eight acoustic signals produced by the speakers, and thus produce a uniform sound field across the wavefront of the vortex, minor adjustments were made to the amplitude of each of the eight signals using a feedback loop to compare the initial amplitude to a new one which included any adjustments made.

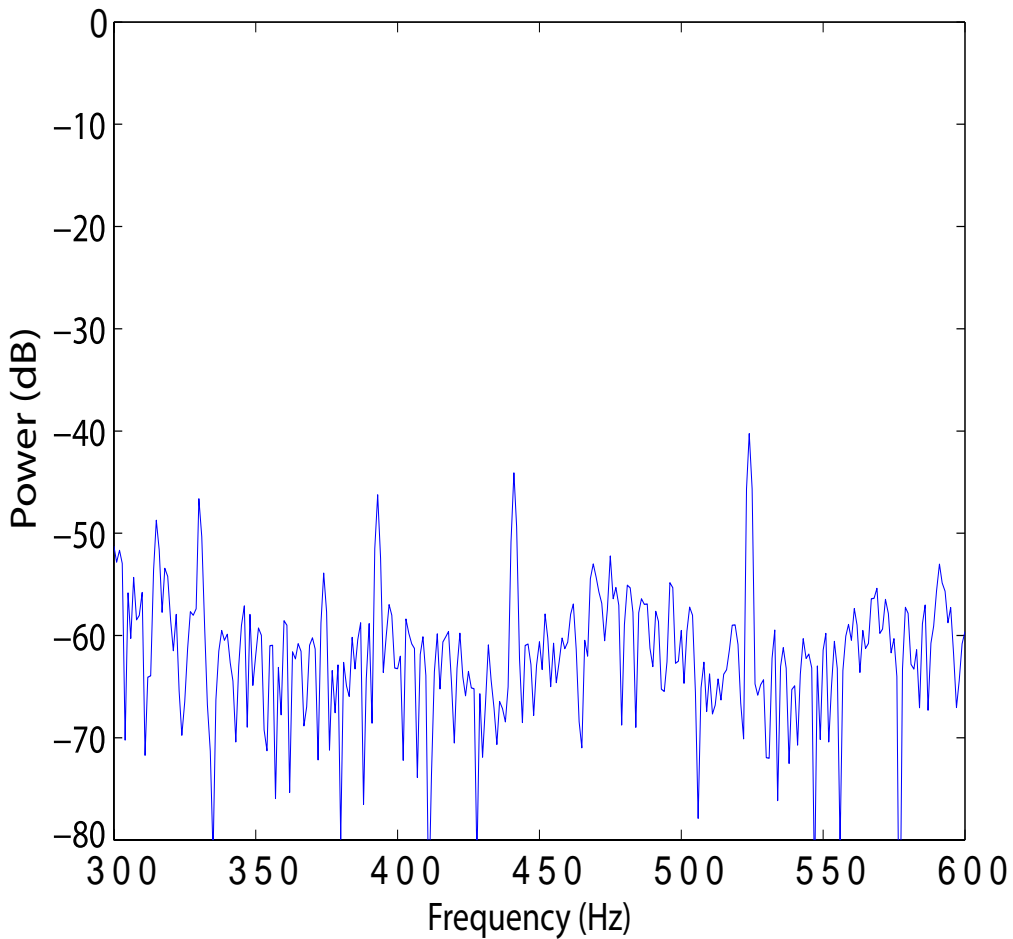


Figure 4.5: Spectral plots of the microphone signal recorded at the on (b) axis position of figure 4.3.

## 4.3 The Experiment

### Polyphonic vortex beam

In order to generate acoustic vortices containing multiple spectral components, a method similar to that used to generate single tone vortices in the work described in chapter 3 was employed. All eight speakers were driven with signals of equal frequency and magnitude,

and by increasing the relative phase delay between adjacent speakers by  $\pi/4$ , a good approximation to an  $\ell = 1$  vortex was attained. The difference between this and previous work was that the monotone vortices were generated using analogue circuitry whereas the polyphonic vortices were created using a digital sound card. This change was implemented because of the difficulty presented by attempting to generate thirty-two separate signals using analogue electronics.

Before measurements could be taken, the output from the speakers had to be normalized. This was achieved by measuring the output from a single frequency (523Hz) across all speakers and adjusting the input amplitude until all eight outputs were identical. Further adjustment was required as the individual components were found to be misaligned by a few millimetres each. The drive voltage to each speaker was again adjusted to be near the maximum permitted ensuring that most measurements were made well above the noise floor of the microphone. The voltage  $V(\nu)_N$ , of the  $\nu$  frequency component, driving the  $N$ th speaker at azimuthal position  $\theta_N$ , is given by

$$V(\nu)_N = A(\nu)(1 + \delta x_\nu \sin \theta_N + \delta y_\nu \cos \theta_N) \sin(2\pi\nu t) \quad (4.1)$$

where  $A(\nu)$  sets the relative amplitude of the vortex field at frequency  $\nu$ . Adjusting the coefficients  $\delta x_\nu$  and  $\delta y_\nu$  for each spectral component allowed the position of the vortex at that frequency to be moved in the transverse plane so that the different frequency components overlapped on the beam axis.

To generate a polyphonic vortex, four sinusoidal signals at

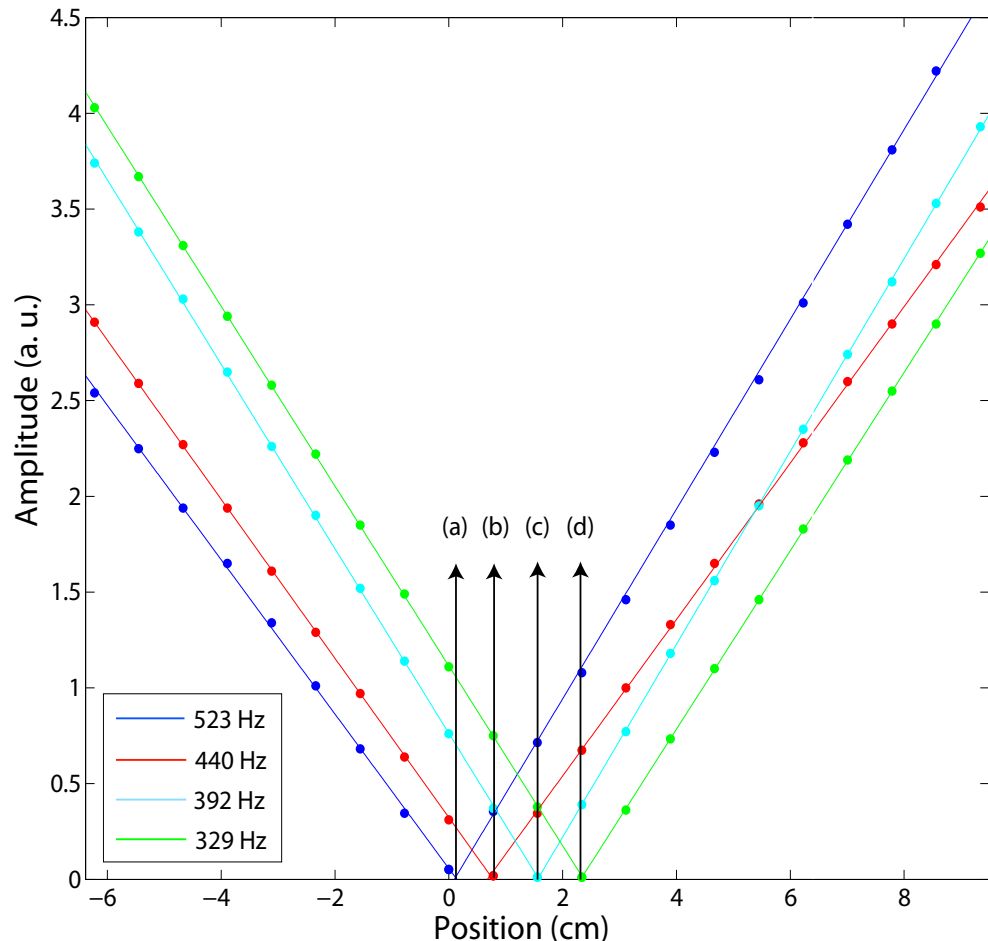


Figure 4.6: Perturbation of the vortex components. The four arrows indicate the positions of the complementary chords of the vortex, and a spectral analysis was made of each point. The results of this analysis can be seen in figures 4.8 to 4.11.

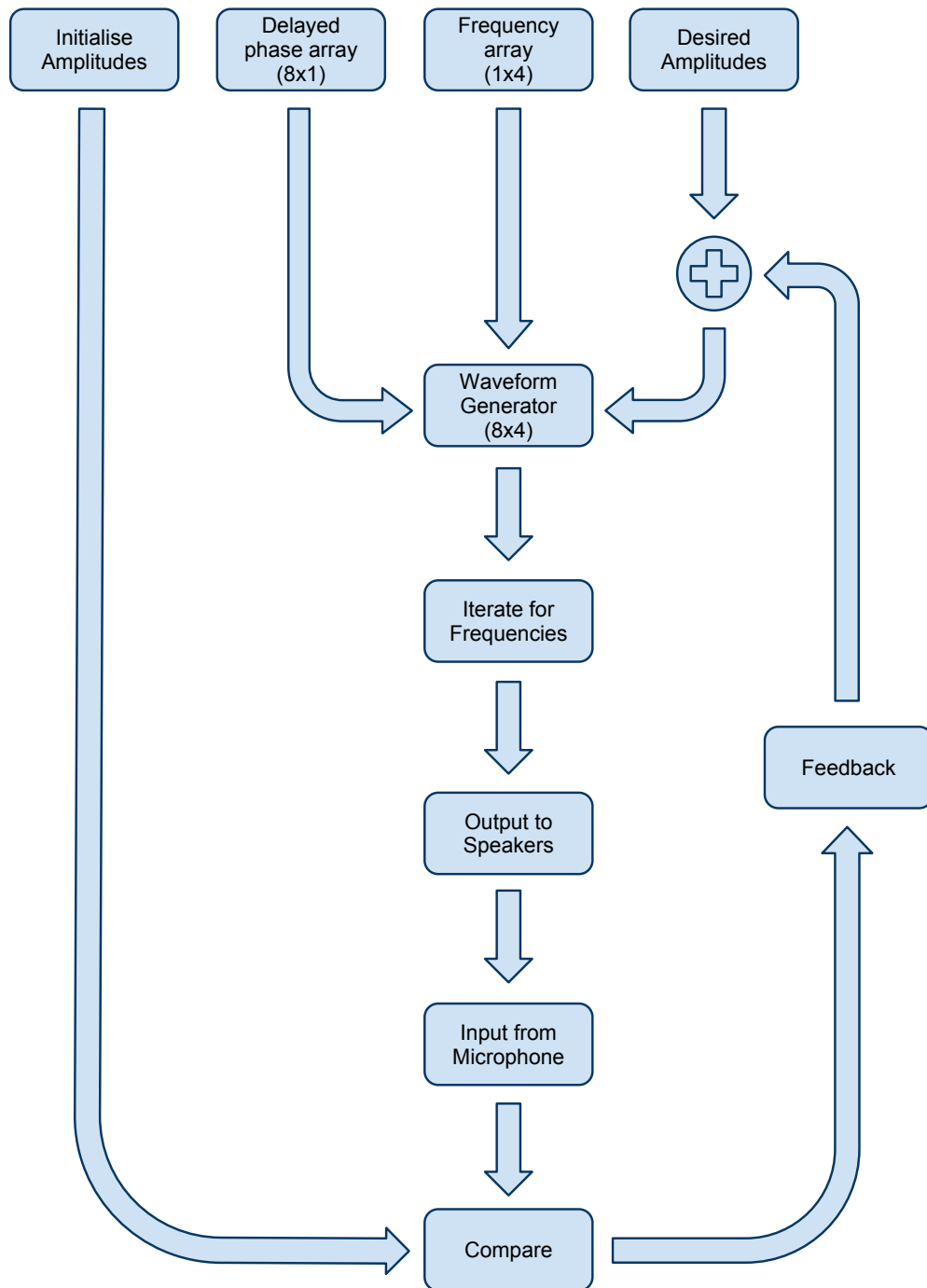


Figure 4.7: Polyphonic vortex algorithm

frequencies of 329Hz, 392Hz, 440Hz, and 523Hz respectively were superimposed upon one another. These frequencies correspond to the notes of E, G, A and C respectively. Successive scans through the vortex core in any direction resulted in similar cross-sections being obtained, although the length of these scans was limited to 60mm on either side of the beam centre by the length of the translation stage. In the region of the singularity, the intensity was expected to scale with  $r^{12\ell}$ . This noise core is of similar origin to that predicted, also for the acoustic case by Berry and Dennis [35]. In their case, the predicted radius of this core was based on a calculation of the ultimate noise floor resulting from the Brownian motion of the air molecules, a sensitivity that cannot be obtained using a conventional microphone. Initially, the electrical noise floor of the microphone was dominated by the acoustic signal from the speakers, but as the drive voltage was reduced, the acoustic signal eventually fell below this floor such that a flat plateau appeared in the centre of the vortex beam 4.1. Note that as the volume is reduced, the area over which the noise dominates increases.

A 1D amplitude cross-section through the polyphonic acoustic vortex can be seen in figure 4.3 with the corresponding spectral plots shown in figures 4.8 to 4.11, while a 2D amplitude cross-section of the four frequencies can be seen in figure 4.2. It was found that, as was expected from an  $\ell = 1$  vortex beam, the acoustic intensity scaled with the square of the intensity of the radius, as indicated by the linear variation in amplitude seen in figure 4.3. The variation in the gradient of the tonal components indicates that the sound beams may well be

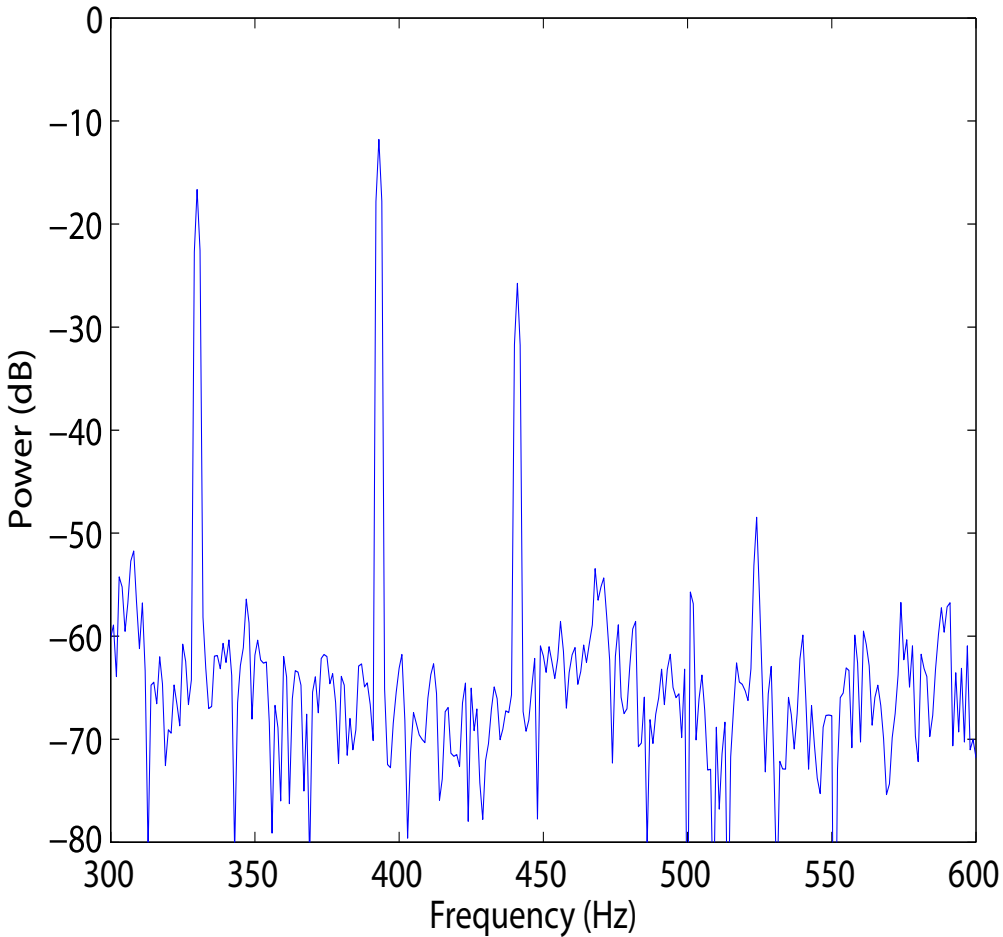


Figure 4.8: Spectral plot of the suppression of the 523 Hz component.

slightly asymmetric at larger distances from the vortex. A suppression of the intensity at the centre of the beam of order 45dB, compared to the equivalent plane wave which was obtained by setting all the relative phases to zero, although this measurement was limited by the measurement sensitivity of the microphone. A spectral analysis made at two different radii can be seen in figures 4.5 and 4.4. The residual spectral signals at the central singularity most probably arise from slight non linearities in the drive electronics.

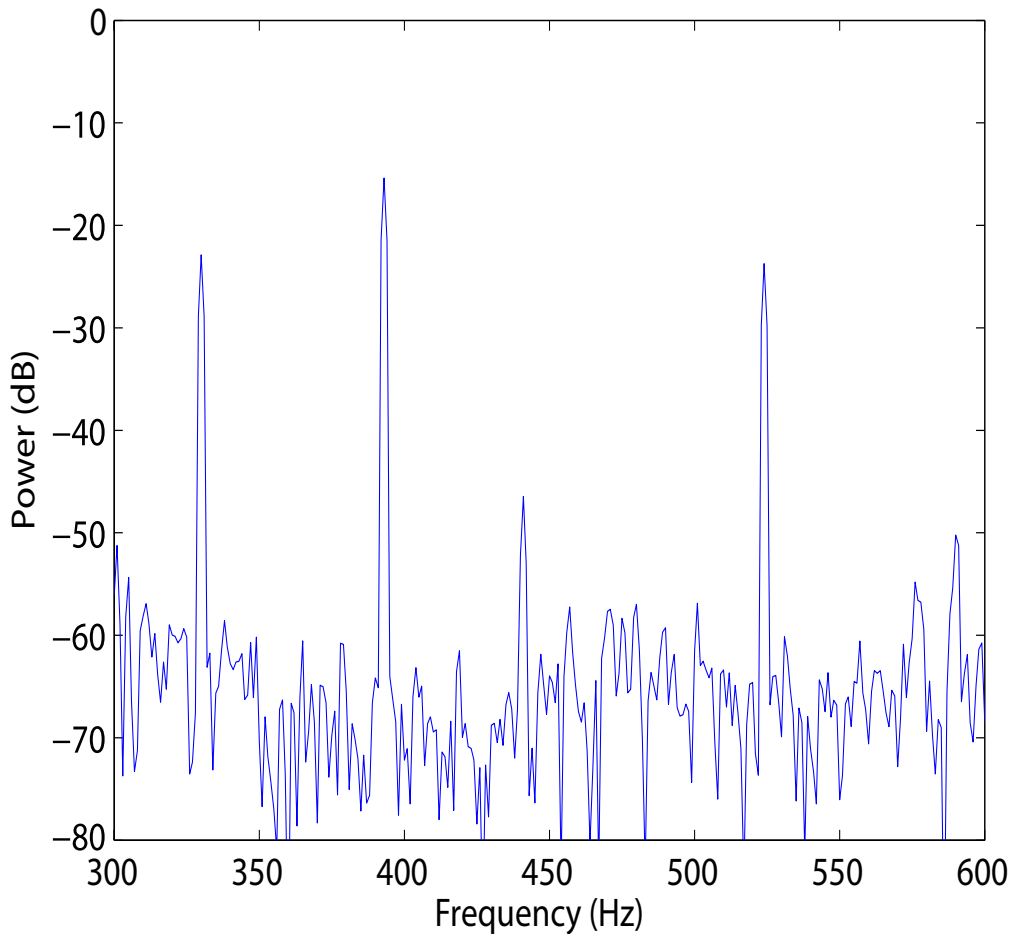


Figure 4.9: Spectral plot of the suppression of the 440 Hz component.

### Perturbing the vortex

Now that a polyphonic acoustic vortex has been generated as an analogue to the optical case, the next step is to investigate whether or not it can be perturbed and see how it compares to a perturbed optical vortex. In the optical case, the perception of colour is highly complex, although it is sufficient to reduce it to a simplistic level and say that the observation of colour is the result of the stimulation of red, green and blue receptors in the eye, or their equivalent pixels on a CCD or CMOS

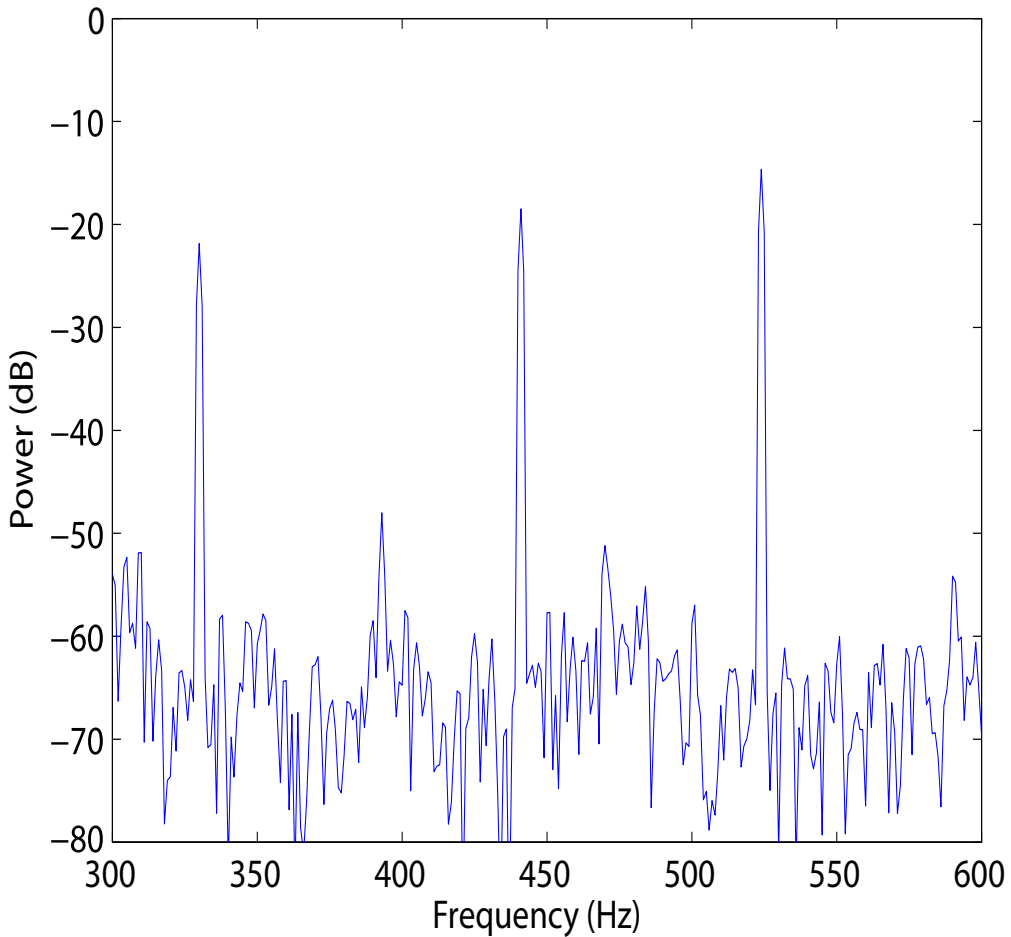


Figure 4.10: Spectral plot of the suppression of the 392 Hz component.

sensor. Complimentary colours, i.e. cyan, magenta and yellow, may be perceived if one of the RGB receptors are absent, as can be seen in the demonstration of a white light vortex where these complimentary colours give a characteristic spatial spectral image [27, 33].

In contrast to this, sound is perceived very differently to light. Whereas light is observed in the form of a spatial pattern in three spectral bins, the human ear can detect multiple acoustic frequencies at a single point. Additionally, whereas a light sensor must make a series of point

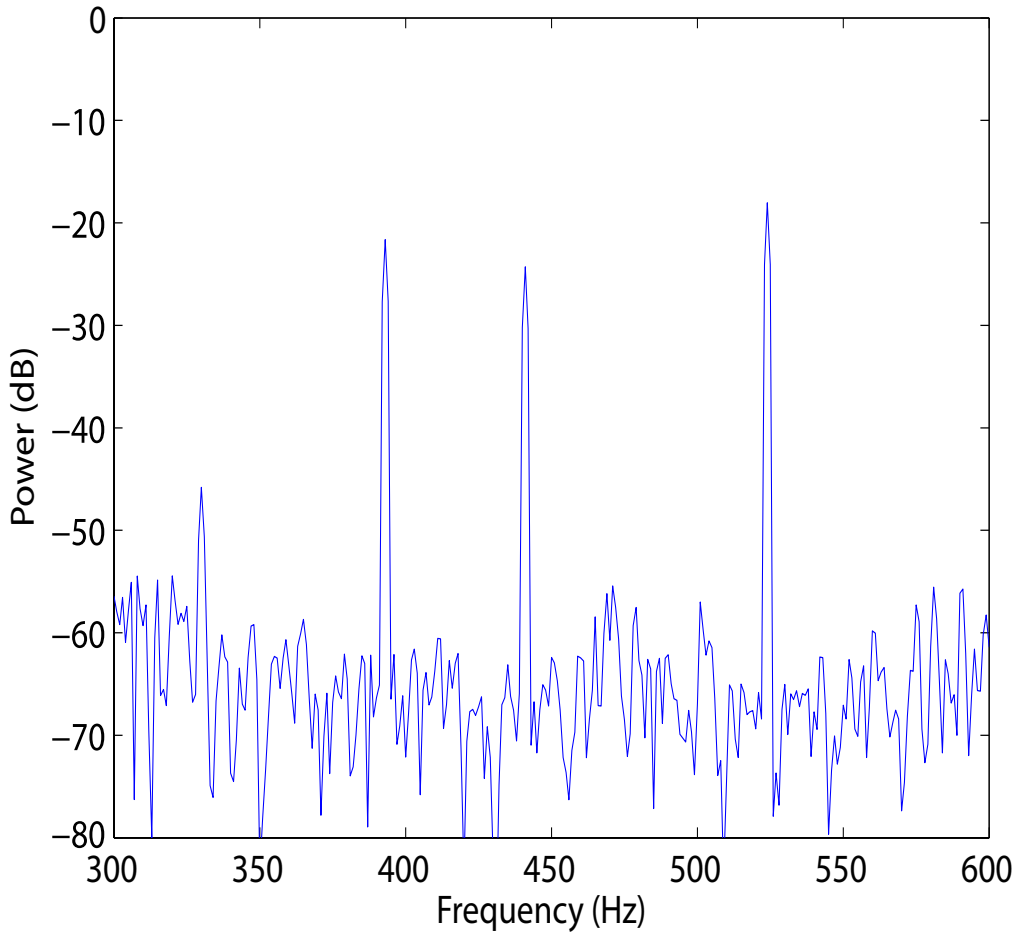


Figure 4.11: Spectral plot of the suppression of the 329 Hz component.

measurements in different locations in order to produce an image, a microphone need only make a single measurement of multiple notes at a single point in order to record a chord. Despite these differences, it is possible to perturb both optical [27] and acoustical vortices in such a way that their constituent components become separated. The tonal components were aligned by adjusting the  $\delta x_\nu$  and  $\delta y_\nu$  elements from equation 4.1 so that they were each separated by a few millimetres 4.6. We note that the applied perturbation causes some distortion of the

form of the beam at larger radii, manifest by a crossing of the straight line fits, indicating a slight beam asymmetry. However, perturbing the vortices in this way does not seem to affect the depth of the intensity null of the vortices themselves. These multiple frequency stimuli are analogous, but obviously not identical, to the complimentary colours comprising multiple wavelengths, hence we term them complimentary chords whose corresponding acoustic spectra are shown in figures 4.8 and 4.11.

# High order phase structures of acoustic vortex beams

## 5.1 Introduction

The work covered in this thesis has been built around the idea that optical beams can carry orbital angular momentum, and that this phenomenon is to be found in both transverse and longitudinal wave fields. The initial work, described in chapter 3 and carried out prior to formal commencement of research, indicated that acoustic waves could not only carry orbital angular momentum, but that they could also transfer it to another medium, in that case a styrofoam disk. The work that followed on from this indicated that these acoustical beams could consist of more than a single tone, and that these tones were independent of one another so that they could be manipulated individually. Through both of these experiments, the presence of orbital angular momentum in the

form of a helical phase front has been deduced from the observations. In this chapter, direct observations of the helical phase structure are presented not only for the first order case, but for the second and fourth orders, as well as the corresponding negative orders.

The experimental apparatus, consisting of the enclosed speaker array (the vortex generator) and the microphone mounted atop a translation stage as described in chapter 2, was arranged as it had been for the polyphonic vortex experiment. A single signal of frequency 440Hz was driven through the speakers using the phase delay method described in previous chapters thus approximating a  $\ell = 1$  vortex. The travelling microphone was moved through the centre of this vortex recording the phase value at various points as it went. After this, the direction of the phase delay was reversed so as to simulate a  $\ell = -1$  beam, and the phase cross-section was recorded in the same manner. In order to generate high-order beams of  $\ell$  values  $\pm 2$  and  $\pm 4$ , the multiplication factor that separated the successive phase values was increased and the phase cross-section was again measured for each beam.

The system design limited the possible values of  $\ell$  which could be achieved due to the use of precisely eight speakers -  $\ell = 3$  was impossible since the number of speakers was not divisible by 3, and the vortex structure would break down at values of 4 or greater ( $\ell = 4$  is included here for reference).

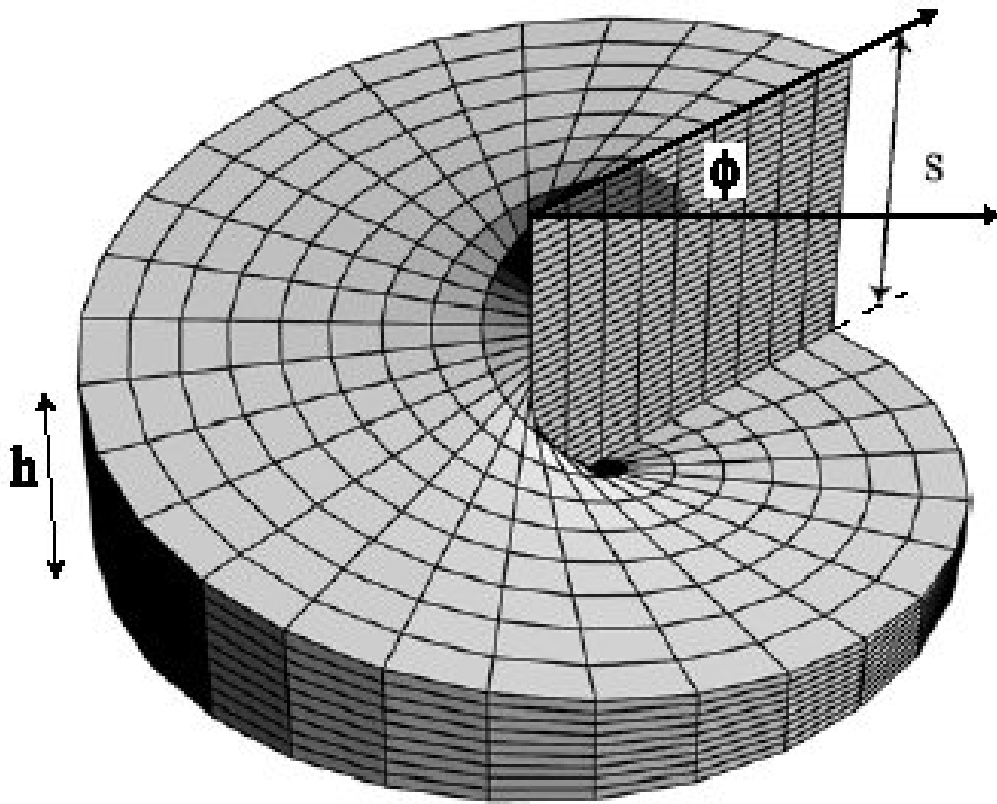


Figure 5.1: A sketch of a spiral phase plate

## 5.2 High order optical beams

Laguerre-Gaussian laser modes are to be found in cylindrically symmetric laser beams and are the natural solution to the paraxial wave equation where a given mode of such a beam is described using the indices  $\ell$  and  $p$  and is denoted  $LG_p^\ell$ . A high order beam is defined as having a mode index  $\ell$  with a non-zero integer value not equal to plus or minus one, however similarly to these low order beams, they do still possess the azimuthal phase term  $\exp(-i\ell\phi)$  that is responsible for the well defined component of orbital angular momentum. Also, like the low-order equivalent, the

amplitude of high order modes,  $E(LG_p^\ell)$ , is defined as

$$\begin{aligned} E(LG_p^\ell) \propto & \exp\left[\frac{-ikr^2z}{2(z_r^2 + z^2)}\right] \exp\left[\frac{-r^2}{\omega^2}\right] \dots \\ & \exp\left[-i(2p + \ell + 1)\arctan\left(\frac{z}{z_r}\right)\right] \dots \\ & \exp[-i\ell\phi][-1]^p \left[\frac{r\sqrt{2}}{\omega}\right]^\ell L_p^\ell\left[\frac{2r^2}{\omega^2}\right] \end{aligned} \quad (5.1)$$

where  $z$  is the distance from the beam waist,  $z_r$  is the Rayleigh range,  $\ell$  and  $p$  are the mode indices,  $k$  is the wave number,  $\omega$  is the radius at which the Gaussian term falls to  $1/e$  of its on-axis value,  $r$  is the radius,  $\phi$  is the azimuthal angle and  $L_p^\ell$  is the generalised Laguerre polynomial.

The first high order optical beams were observed by He *et al* in 1995 [36], three years after the initial observation of single order beams by Allen *et al*, who were able to trap a particle using a third order 'doughnut' beam, and to subsequently rotate the particle using the momentum transfer that has been described earlier in this thesis.

### 5.3 Techniques for generating high-order L-G optical beams

There are various ways in which these beams may be generated. The first is to do so using a laser and a mode convertor. By generating a high-order Hermite-Gaussian mode (one way or another) inside the laser cavity and passing the resultant beam through a mode convertor, a high-order Lauguerre-Gaussian beam may be produced. The mode convertor will introduce a Guoy phase shift on an incident beam that will convert the  $m$

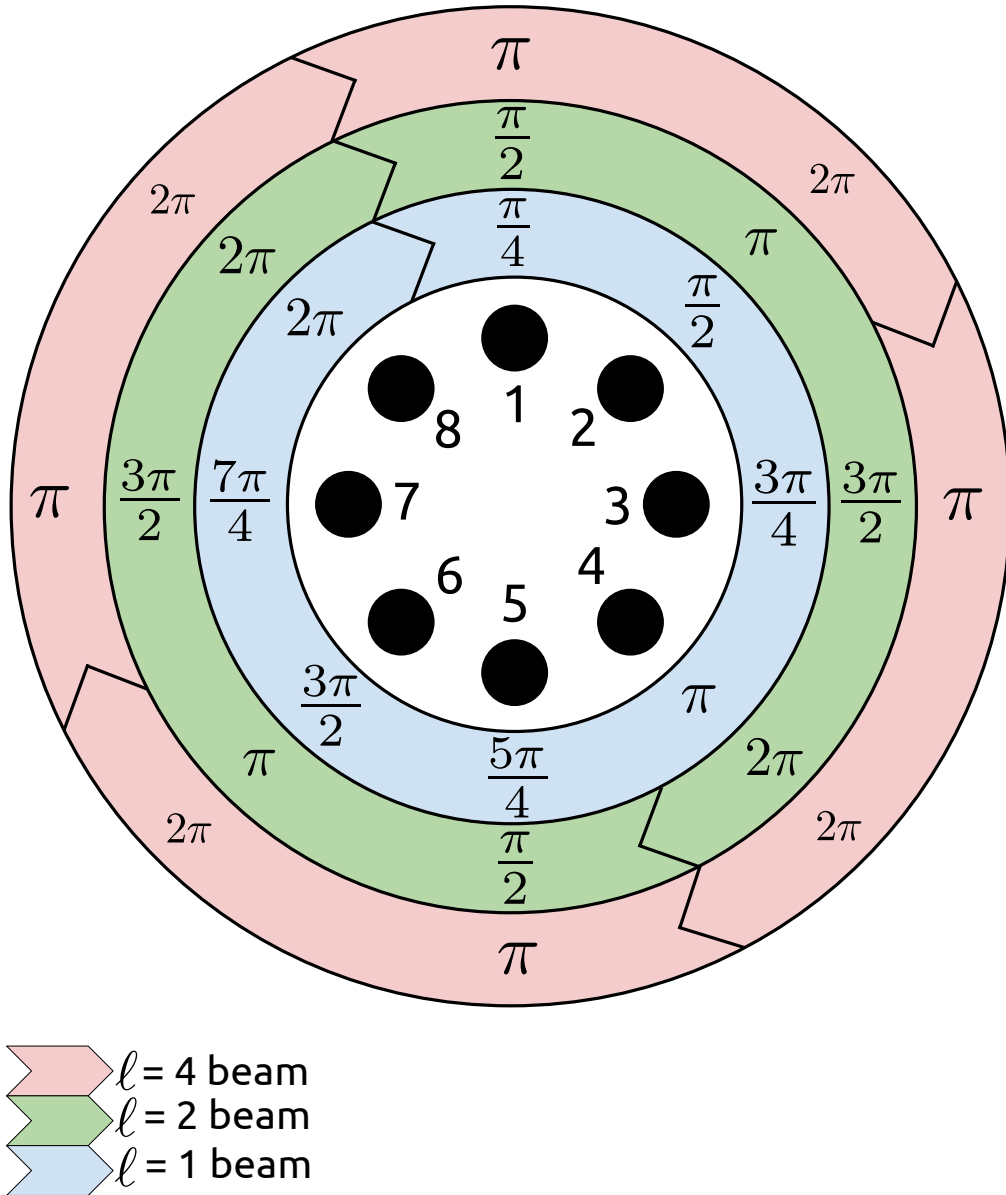


Figure 5.2: A wrapped phase map indicating the phase value measured at each speaker for each value of  $\ell$ .

and  $n$  indices of the Hermit-Gaussian beam to Laguerre-Gaussian indices  $\ell$  and  $p$  with a conversion of  $\ell = (m - n)$  and  $p = \min(m, n)$ . The downside to this method is that the laser must be capable (or be made

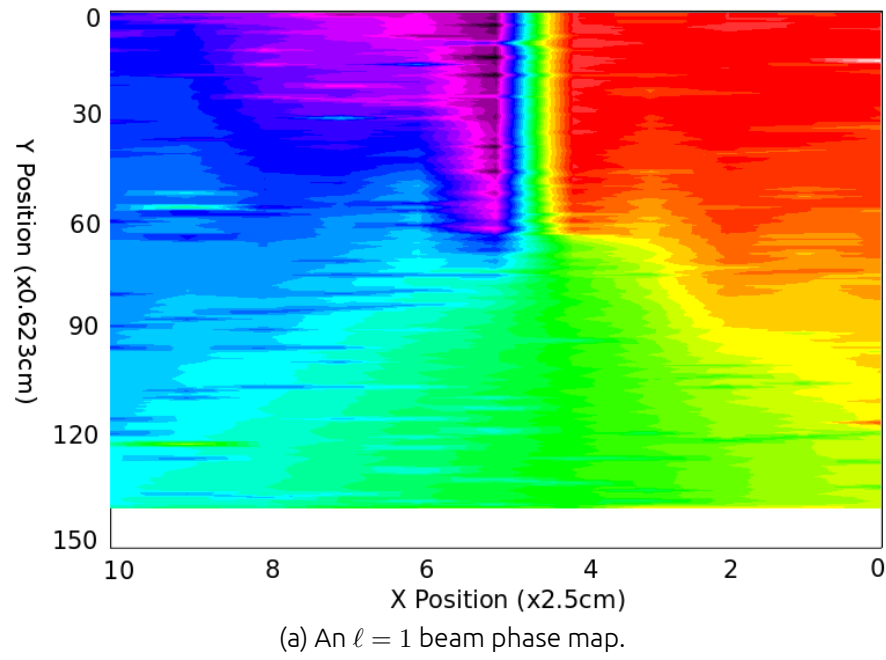
to be capable) of generating high-order Hermite-Gaussian modes, which is outwith the ability of many types of laser.

The two other techniques that may be employed int he generation of high-order Laguerre-Gaussian modes are: computer generated holograms; and spiral phase plates. Using the latter method, a fundamental Gaussian beam is incident upon a plate of either crystal or plastic disk with an increasing thickness around it's circumference, as can be seen in figure 5.1<sup>1</sup>. In this particular case, the value of  $s$  is calculated to be  $(n - 1)/\lambda\ell$  where  $n$  is the refractive index of the material from which the plate is constructed,  $\lambda$  is the wavelength of the incident light and  $\ell$  is the desired azimuthal charge. Using this experession, a value of  $s$  is obtained that is precisely a whole number of wavelenghts thick, with respect to the incident light. The obvious drawback to this method is that the plates are not only limited to use with a single wavelength of light and to generate a single value of  $\ell$ , but due to the very precise calculations involved, the devices must be precision engineered which makes them incredibly expensive. High-order beams are generated using a plate with a number of spirals equal to the order of beam desired.

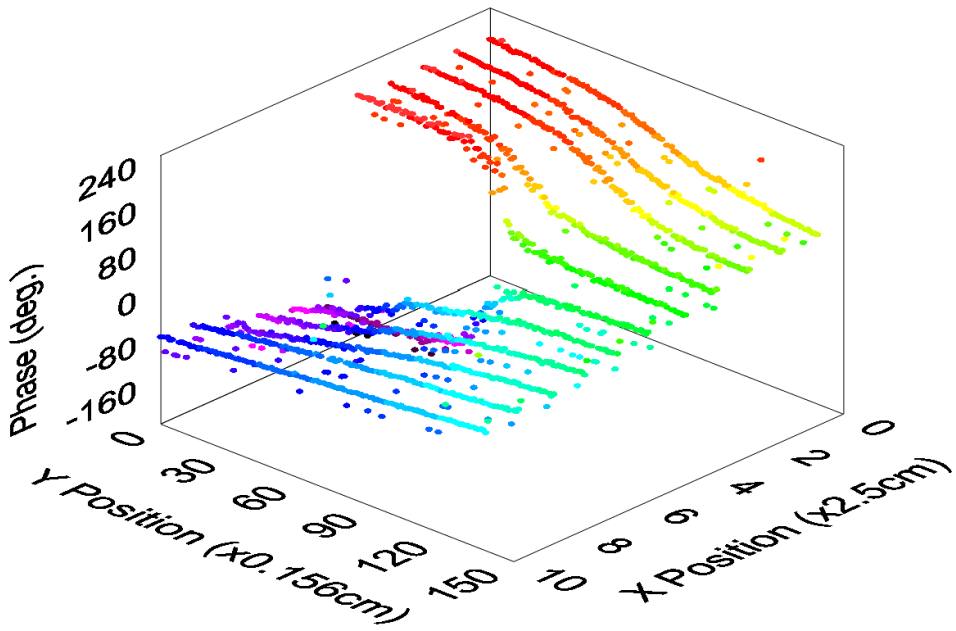
To generate a simple hologram, the diffraction pattern of an electromagnetic field of interest and a static reference field is recorded. To apply this method to a the generation of a Laugerre-Gaussian beam, the two fields must produce a forked diffraction pattern with  $\ell$  dislocations, which results in a screw phase dislocation along the beam axis. The structure of the forked hologram can be determined using the

---

<sup>1</sup>Figure attributed to <http://iopscience.iop.org/1367-2630/6/1/071/fulltext>



(a) An  $\ell = 1$  beam phase map.



(b) An  $\ell = 1$  beam

Figure 5.3: An  $\ell = 1$  beam.

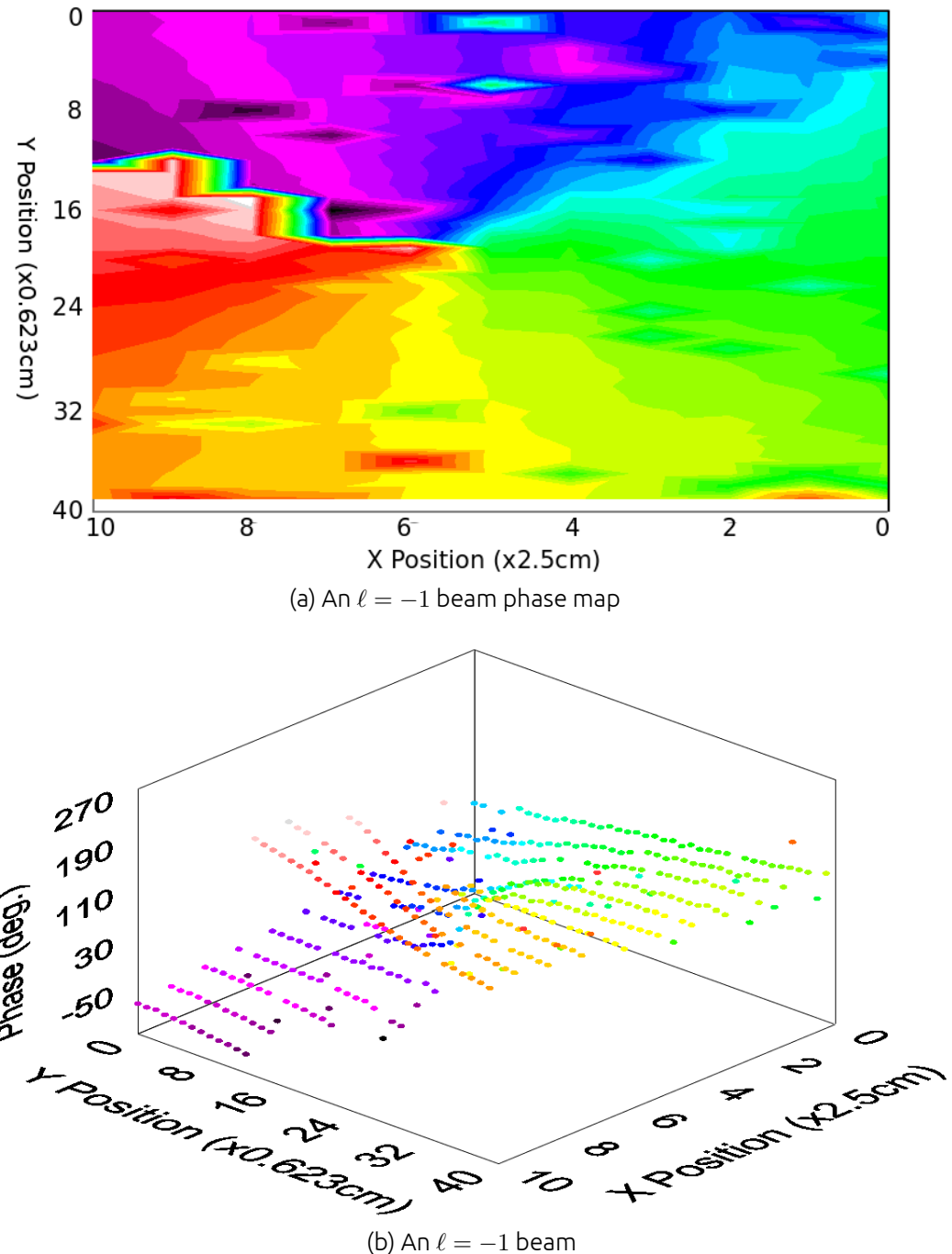


Figure 5.4: An  $\ell = -1$  beam.

following expression illustrating the boundary between the transparent and opaque areas of the hologram

$$\ell \frac{\phi}{\pi} = n + \frac{2r}{\Lambda} \cos\phi \quad (5.2)$$

where  $r$  and  $\phi$  are the polar coordinates,  $\ell$  is the desired topological charge and  $\Lambda$  is the grating period. A fundamental Gaussian beam incident upon the point of the pattern at which the fork begins will be transformed into a superposition of an infinite number of Laguerre-Gaussian beams with identical  $\ell$  values and different  $p$  values. It can be shown that the  $p = 0$  mode contributes 78.5% of the intensity in the first diffracted order. The contribution of higher order LG modes, where  $p \neq 0$  can be determined by

$$E_{\ell p} = \sqrt{\frac{p!}{(p+1)!}} \frac{\ell \Gamma(p + \frac{1}{2})}{2p!} \quad (5.3)$$

This expression is dependent on the identicity of the input and output beam waists.

## 5.4 Higher order acoustical beams

### Generation

The generation of the high order acoustical beams describes in this chapter followed a similar method to that employed in the generation of the first order beams described in previous chapters. The same apparatus described in chapter 2 was used in much the same fashion as it was in chapters 3 and 4. The labview script that was used to generate the first

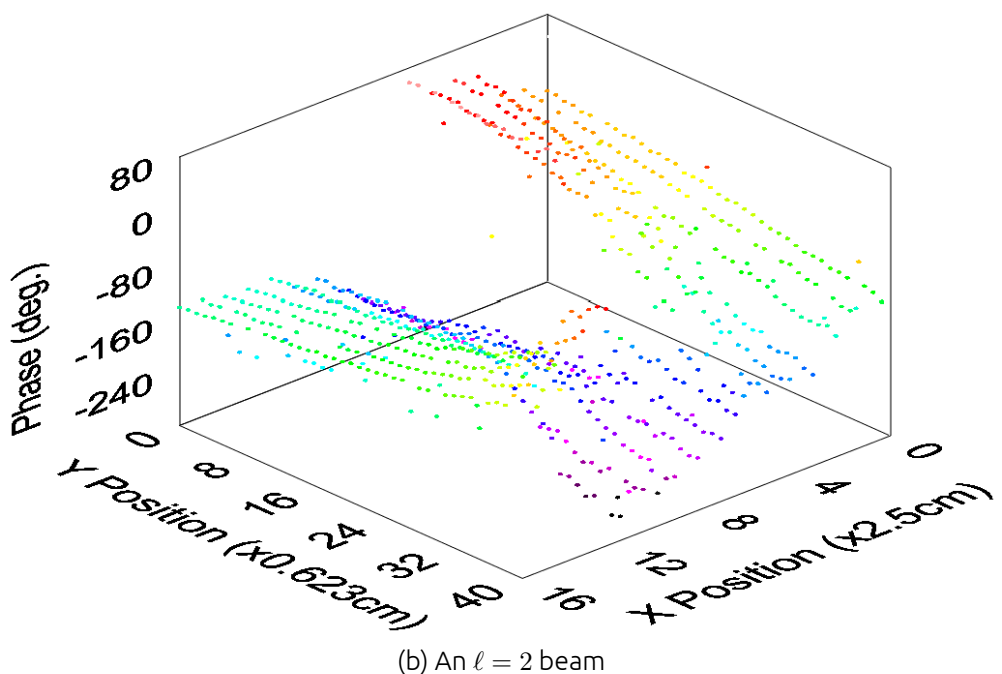
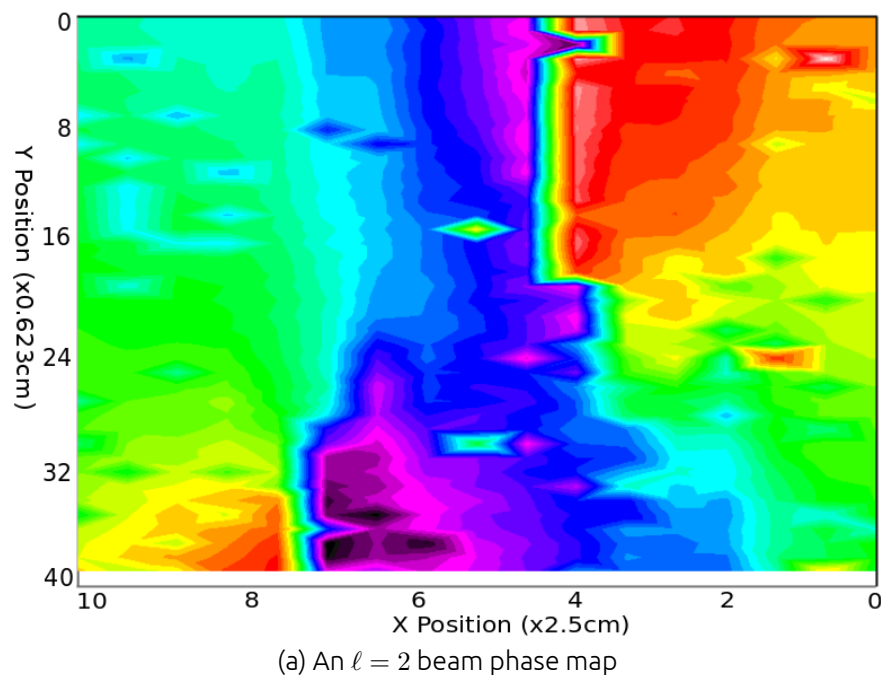


Figure 5.5: An  $\ell = 2$  beam

order beams was written with an adjustable  $\ell$  value programmed into it, meaning that no rewrite of the code was necessary in order to produce high order beams.

The generation of the phase values that were to be fed to the sound card was the very first thing that happened in the LabView program. A simple *for* loop that iterated 8 times was executed. Into this loop was past the chosen value of  $\ell$  and the expression

$$\phi = \frac{n\ell\pi}{m} \quad (5.4)$$

was evaluated, where  $n$  is an integer denoting the current iteration of the loop has takes the values of 1 to 8 inclusive and  $\ell$  is the topological charge of the vortex that is being generated and  $m$  is half the number of speakers being user, in this case 4. The eight element array of phase values that was produced in this way was then used to generate an eight element array of sinusoidal signals which were sent to each of the eight speakers in turn

Figure 5.2 illustrates the phase value recorded at each speaker for each value of  $\ell$ . The innermost right describes the phase of an  $\ell = 1$  beam. The phase of each speaker is separated by a value of  $\pi/4$  which, for eight speakers, results in a sum change of  $2\pi$  between the first and eighth speakers. The middle ring shows the phase for a  $\ell = 2$  beam. Each speaker in this case has a phase differential of  $\pi/2$  with respect to the preceeding and proceeding speakers, resulting in a  $2\pi$  phase difference between the first and fourth speakers. The phase is then wrapped round to 0 so that when it is measured at the fifth speaker, a result of  $\pi/2$

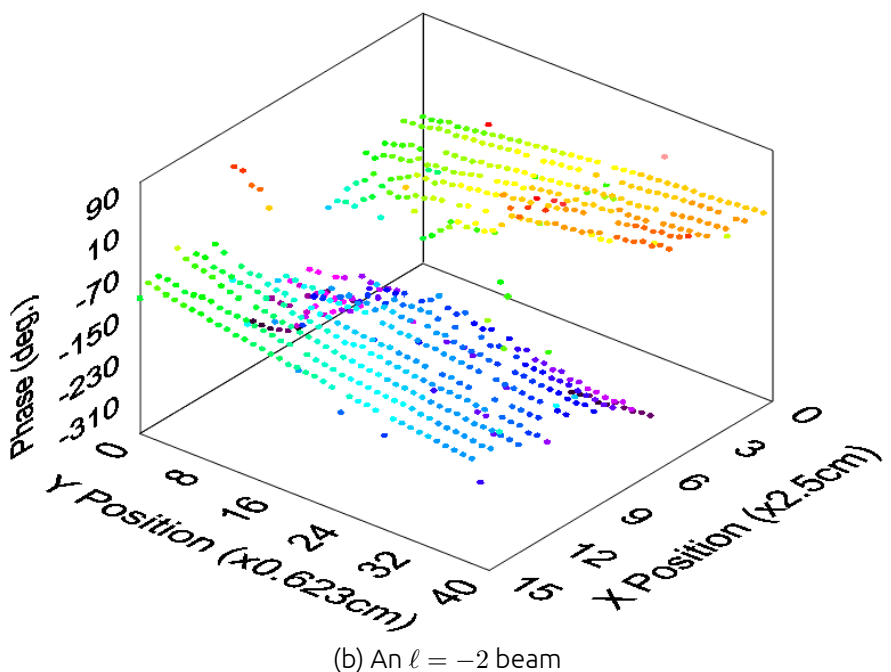
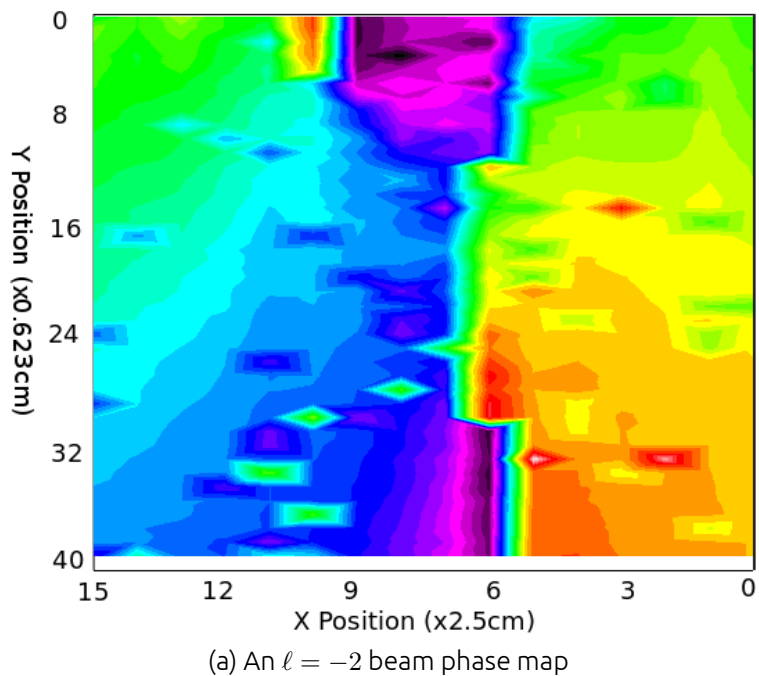


Figure 5.6: An  $\ell = -2$  beam

is obtained, resulting in a  $2\pi$  differential between the fifth and eighth speakers. The overall effect observed is that of a helically phased beam with two discreet phasefronts. The same effect is observed for an  $\ell = 4$  beam.

A  $\ell = 3$  beam has not been demonstrated as the construction of the speaker array limited the range of  $\ell$  values we could produce. Equation 5.4 indicates the phase value that should be recorded at each speaker, however for a  $\ell = 3$  beam to be fully constructed with  $0 \leq \phi \leq 2\pi$ , the  $\ell$  values must be a factor of the number of nodes used to construct the beam. In this case, a ninth speaker must be added to the system so that three sets of three speakers produce phase values of  $2\pi/6$ ,  $2\pi/3$  and  $2\pi$ . While including a ninth speaker would facilitate the generating of a  $\ell = 3$  beam, it would interfere with the generation of  $\ell = 2, 4$  beams since the use of an odd number of speakers would leave the  $\ell = 2, 4$  beams with the problem that the ninth speaker solved for  $\ell = 3$ . This would however be negated through the use of an array of speakers large enough to mask the presence/absence of an odd speaker.

## Observation

As with the previous experiments, the apparatus has remained unchanged for this investigation. A monotone waveform was generated in labview possessing a frequency of 440Hz. This signal was split into eight constituent components to each of which a relative phase delay was applied such that an integer number of  $2\pi$  rotations of the phase

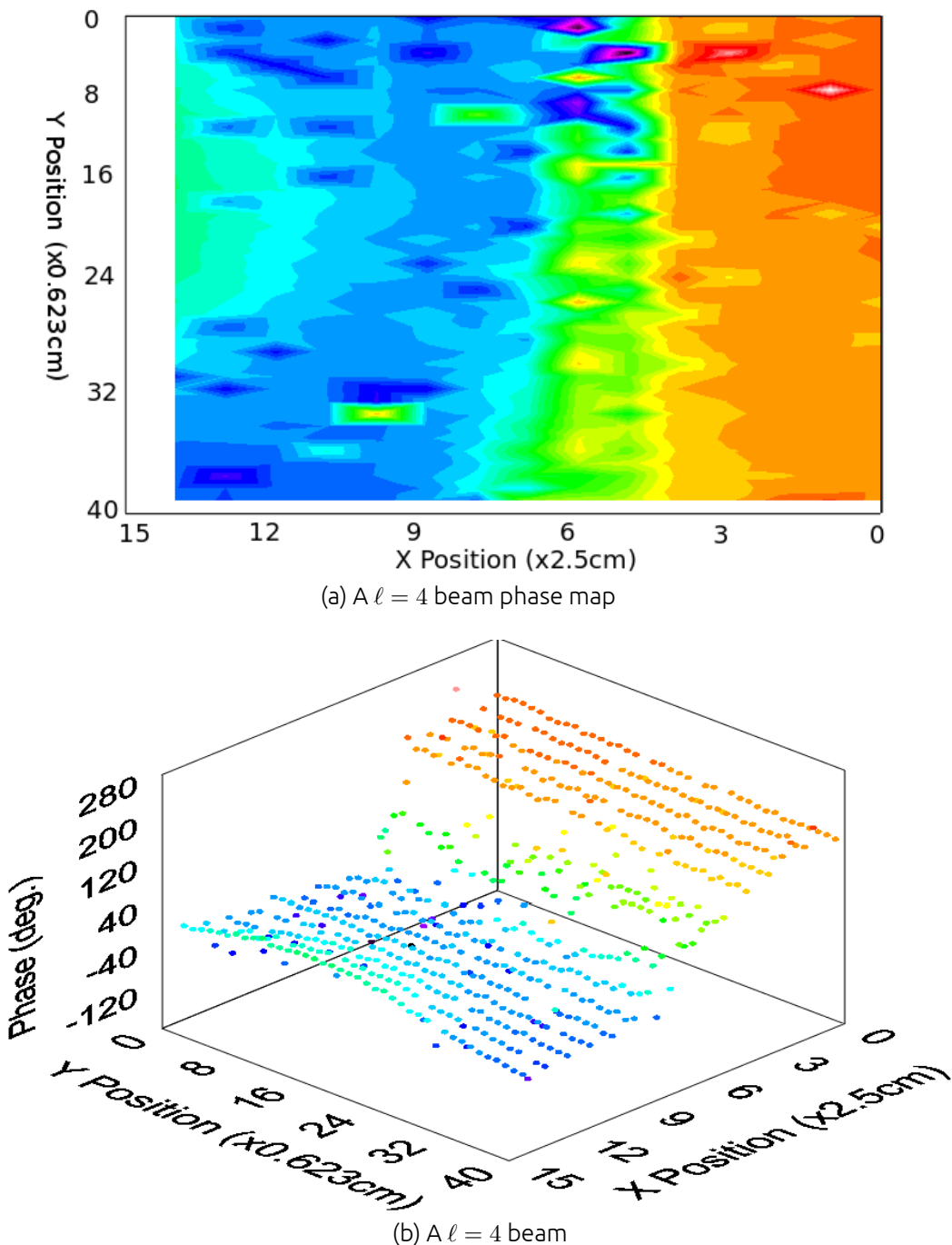


Figure 5.7: A  $\ell = 4$  beam

about the original were produced. The signal was then send to the Motu 828mkIII which, using the amplifier deck connected to the speaker array, drove the signal to the speakers and thus produced a monophonic acoustical beam with an adjustable mode index. The microphone and translation stage from previous experiments was used to measure the phase value of the generated beam. By tranversing the microphone accross the width of the beam on the translation stage, a cross-section of the beam's phase profile may be measured. By doing this for multiple lateral positions, it was possible to stitch together these two dimensional figures in order to produce a three-dimensional plot of the beams phase structure. The following figures illustrate these results. It should be noted that the reader will observe a rapid change in phase at the point at which the portion of the beam with the higher phase value approached the same z-coordinate occupied by the portion of the beam with the lower phase value. This is an issue with Labview's rendering of the figures and should be disregarded.

The experiments in chapters 3 and 4 were each carried out using  $\ell = 1$  beams, for the simple reason that nothing more complicated was required at the time. Figures 5.3 and 5.4 depict beams of mode index  $\ell = \pm 1$ .

As has been mentioned previously, the experimental arrangement consisted of eight speakers in a circular arrangement, and that the acoustical vortices are generated by driving each speaker with a separate signal with an appropriate phase delay between consecutive speakers, thus giving an acceptable approximation to the desired beam.

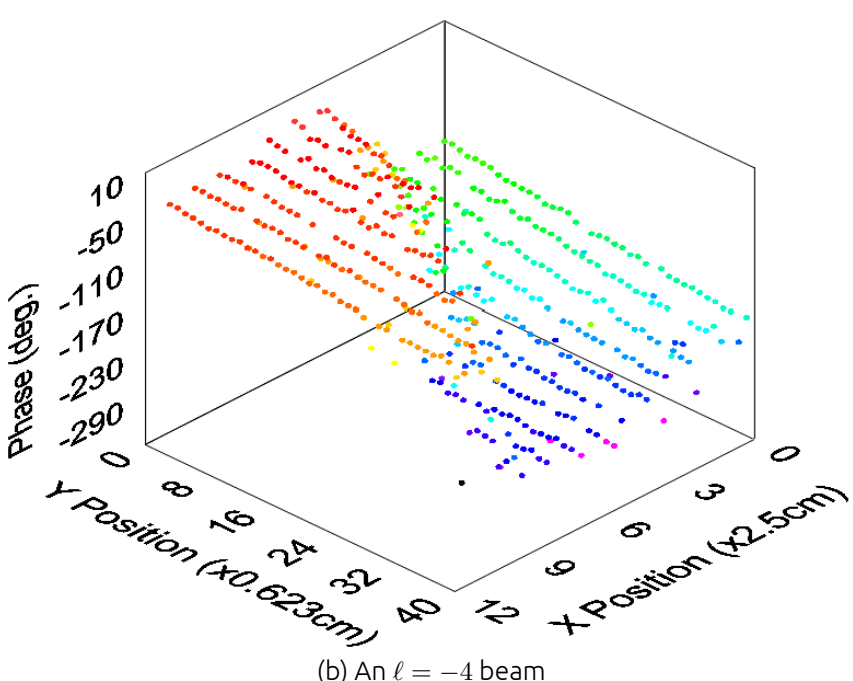
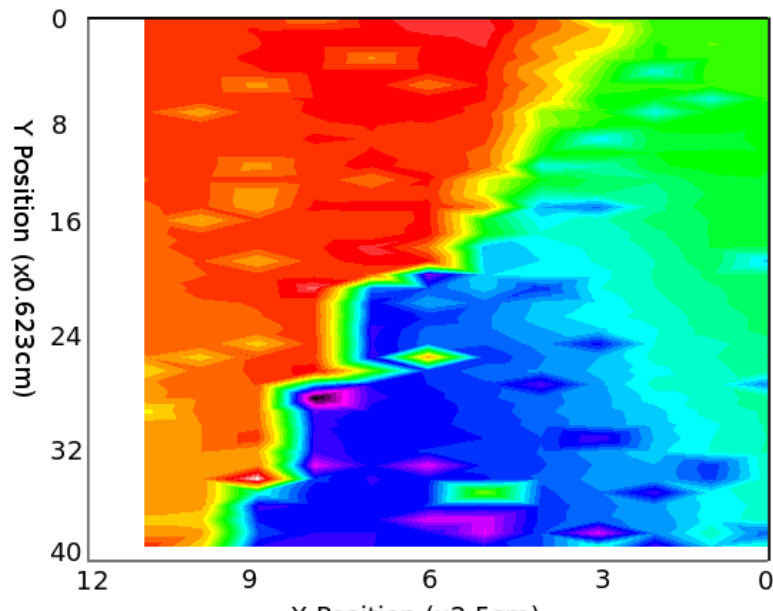


Figure 5.8: A  $\ell = -4$  beam

This system is not without its limitations however. A beam of mode index  $\ell = 3$  was altogether impossible to produce without a ninth speaker in the arrangement. It was however possible to produce a  $\ell = 4$  beam with this number of speakers, however this is the point at which the results begin to break down as the relative phase delay between each speaker has to be  $\pi$ , which means that it is impossible to discern a  $\ell = 4$  beam from a  $\ell = -4$ . Results for supposed  $\ell = \pm 4$  beams can be seen in figures 5.7a to 5.8b, and without the caption, it is possible that one of these figures might simply be the other reversed along the x-axis.

Figure 5.5a to ?? illustrate the phase profile for  $\ell = \pm 2$  beams.

# 6

## CHAPTER

## Conclusions

The motivation behind this thesis, and the work contained therein, was to illustrate the equivalence of transverse and longitudinal wavefields in the context of certain phenomena already known to have been observed in the former.

The main body of work was inspired by a previous experiment carried out by the author. The idea of an 'optical spanner', upon which the initial experiment was based, is simply a specific application of the concept of using light to manipulate matter, and was first demonstrated using a beam of circularly polarized light. Since that initial observation, many experiments have been carried out using such beams, all of which have been conducted around, and dependent upon, the idea of transverse EM waves possessing a particular polarization. Sound, however, is a longitudinal beam, and thus cannot be polarised which prohibits it from possessing the component of spin angular momentum upon which the manipulation of matter, including the use of the optical

spanner, is dependent.

On the other hand, longitudinal waves do possess a component of orbital angular momentum, and it is with this component that an acoustic spanner was able to be assembled. By assembling a circular array of eight loudspeakers and driving them each with a signal that is identical in every aspect except that each one is  $\pi/4$  out of phase with respect to the previous one, an approximation to a  $\ell = 1$  vortex was generated. A styrofoam disk was suspended above the speaker array and when the speakers were activated, the disk was observed to be set into motion, accelerating upon its axis until the suspension wire could rotate no further. Switching the direction of the phase difference resulted in the disk rotating in the opposite direction with an equal acceleration and stopping at the same maximum displacement. These observations were taken as the strongest possible proof that acoustic waves could be utilised in the manipulation of matter in the same manner as optical waves.

The confirmation of this result allowed us to consider the possibility of polyphonic acoustical beams, and more importantly, the possibility of separating the out the constituent tones so as to produce multiple acoustic traps. Using the same apparatus as in the monophonic experiment, a signal consisting of the superposition of four monophonic tones was used to drive the speakers. A microphone mounted on a translation stage was used to measure a cross-section of the intensity field of the resultant vortex which, when passed through a spectrum analyser, revealed the existence of four distinct concentric vortices, each corresponding to one of the four tones used to construct the driving

signal.

The input signal was then perturbed in such a way as to decrease the intensity measured at one particular speaker while imparting an equal but negative adjustment at the speaker directly opposite the affected speaker. The value of the adjustment was deliberately varied from one constituent signal to the next. The cross-section was remeasured and the four component vortices were observed to have separated from one another, providing confirmation that the monotone acoustic spanner could indeed be extended to utilize multiple traps, though in this experiment no attempt was made to trap multiple objects using this beam.

The final part of this investigation was an attempt to directly measure the phase profile of the monophonic beam used in the first experiment. Resetting the driving signal to what was initially, a monophonic vortex, similar to that used to demonstrate the acoustic spanner, was produced and multiple cross-sections of the intensity field were measured. The initial measurement was made at the far side of the speaker array, and subsequent measurements were made from regular positions closer and closer to the opposite side. This way, enough data points could be collected to produce a 3D model of the phase front of the beam with a suitable level of detail. Colour-mapping the surface of this model allowed for easy observation of the phase structure of the beam under investigation.

Using this method, the phase structure of beams of increasing  $\ell$  value was measured and observed up to and including  $\ell = 4$ . In order to

produce such beams, the phase difference between adjacent speakers was adjusted so that, for  $\ell = 2$ , the phase difference was increased to  $\pi/2$  for the first four speakers, before the phase was wrapped back round to zero after the fourth speaker. For  $\ell = 4$ , measurements were taken however the phase structure of the beam could not be observed since only two speakers were being used to produce each helix, which was insufficient for the construction of a helically phased beam. Measurements were also made of the negative  $\ell$  value for each positive value measured, and the measured phase fronts were observed to be of equal and opposite value to their positive counterparts.  $\ell = 3$  was not measured due to the limitations of the apparatus.

The study detailed in this thesis was devised as a means of determining the equivalence of longitudinal and transverse waves in certain key areas, namely those phenomena leveraged in the construction and operation of optical tweezers. The success of this investigation has laid a foundation upon which may, in the future, be built a fully functioning set of acoustic tweezers. The acoustic spanner has already proven that such a device is practical, the manipulation of the constituent vortices of the polyphonic vortex illustrates the potential for multiple traps and the measurement of the phase fronts of high-order acoustic beams proves that more complex wavefronts are possible in such a system. The science behind the construction and operation of a set of acoustic tweezers has been thoroughly investigated in this work, and now the only challenge remaining to the realisation of such a device is an engineering one.

# Publications

K. D. Skeldon, C. Wilson, M. Edgar and M. J. Padgett. *An acoustic spanner and its associated rotational Doppler shift.* *New J. Phys.* **10** 013018 (2008).

C. Wilson, M. J. Padgett. *A polyphonic acoustic vortex and its complimentary chords.* *New. J. Phys.* **12** 023018 (2010).

C. Wilson, M. J. Padgett. *Monophonic and polyphonic acoustic vortices.* International conference on orbital angular momentum. York (2010).

# Bibliography

- [1] J. H. Poynting. The wave motion of a revolving shaft, and a suggestion as to the angular momentum in a beam of circularly polarised light. *Proc. Roy. Soc. A*, 82(557):560, Jun 1909.
- [2] R. A. Beth. Direct detection of the angular momentum of light. *Phys. Rev.*, 48(5):471, Sep 1935.
- [3] J. F. Nye and M. V. Berry. Dislocations in Wave Trains. *Proceedings of the Royal Society of London. A. Mathematical and Physical Sciences*, 336(1605):165–190, 1974.
- [4] L. Allen, M. V. Beijerbergen, R. J. C. Spreeuw, and J. P. Woerdeman. Orbital Angular Momentum and the Transformation of Laguerre-Gaussian Laser Modes. *Phys. Rev. A*, 45(11):8185–8189, Jun 1992.
- [5] D. M. Ceperley. Path-integral calculations of normal liquid  $^3\text{He}$ . *Phys. Rev. Lett.*, 69(2):331–334, Jul 1992.
- [6] A. O. Santillán and K. Volke-Sepúlveda. A demonstration of rotating sound waves in free space and the transfer of their

- angular momentum to matter. *AMERICAN JOURNAL OF PHYSICS*, 77(3):209–215, MAR 2009.
- [7] K. D. Skeldon, C. Wilson, M. Edgar, and M. J. Padgett. An acoustic spanner and its associated rotational doppler shift. *New J. Phys.*, 10:013018, January 2008.
- [8] C. Wilson and M. J. Padgett. A polyphonic acoustic vortex and its complementary chords. *New J. Phys.*, 12:023018, February 2010.
- [9] A. T. O’Neil, I. MacVicar, L. Allen, and M. J. Padgett. Intrinsic and extrinsic nature of the orbital angular momentum of a light beam. *Phys. Rev. Lett.*, 88(5), Feb 2002.
- [10] M. E. McIntyre. On the myth. *Journal of Fluid Mechanics*, 106(-1):331–347, 1981.
- [11] J. Lekner. Acoustic beam invariants. *Phys. Rev. E*, 75(3):036610, Mar 2007.
- [12] B. T. Hefner and P. L. Marston. An acoustical helicoidal wave transducer with applications for the alignment of ultrasonic and underwater systems. *The Journal of the Acoustical Society of America*, 106(6):3313–3316, 1999.
- [13] J-L. Thomas and R. Marchiano. Pseudo angular momentum and topological charge conservation for nonlinear acoustical vortices. *Phys. Rev. Lett.*, 91(24):244302, Dec 2003.

- [14] R. Marchiano and J-L. Thomas. Synthesis and analysis of linear and nonlinear acoustical vortices. *Phys. Rev. E*, 71(6):066616, Jun 2005.
- [15] Bazhenov, V. Y. and Vasnetsov, M. V. and Soskin, M. S. Laser beams with screw dislocations in their wavefronts. *JETP Lett.*, 52:429–31, 1990.
- [16] N. R. Heckenberg, R. McDuff, C. P. Smith, and A. G. White. Generation of optical phase singularities by computer-generated holograms. *Opt. Lett.*, 17(3):221–223, 1992.
- [17] S. Gspan, A. Meyer, S. Bernet, and M. Ritsch-Marte. Optoacoustic generation of a helicoidal ultrasonic beam. *JOURNAL OF THE ACOUSTICAL SOCIETY OF AMERICA*, 115(3):1142–1146, MAR 2004.
- [18] Karen Volke-Sepúlveda, Arturo O. Santillán, and Ricardo R. Boullosa. Transfer of angular momentum to matter from acoustical vortices in free space. *Phys. Rev. Lett.*, 100(2):024302, Jan.
- [19] B. A. Garetz. Angular doppler effect. *J. Opt. Soc. Am.*, 71(5):609–611, 1981.
- [20] R. D'E. Atkinson. Energy and angular momentum in certain optical problems. *Phys. Rev.*, 47(8):623–627, Apr 1935.
- [21] J. Courtrial, D. A. Robertson, K. Dholakia, L. Allen, and M. J. Padgett. Rotational frequency shift of a light beam. *Phys. Rev. Lett.*, 81(22):4828–4830, Nov 1998.

- [22] P. Coullet, L. Gil, and F. Rocca. Optical vortices. *Optics Communications*, 73(5):403 – 408, 1989.
- [23] I. V. Basistiy, V. Yu. Bazhenov, M. S. Soskin, and M. V. Vasnetsov. Optics of light beams with screw dislocations. *Optics Communications*, 103(5-6):422 – 428, 1993.
- [24] J. Masajada and B. Dubik. Optical vortex generation by three plane wave interference. *Optics Communications*, 198(1-3):21 – 27, 2001.
- [25] K. O'Holleran, M. J. Padgett, and M. R. Dennis. Topology of optical vortex lines formed by the interference of three, four, and five plane waves. *Opt. Express*, 14(7):3039–3044, 2006.
- [26] K. O'Holleran, M. R. Dennis, F. Flossmann, and M. J. Padgett. Fractality of light's darkness. *Phys. Rev. Lett.*, 100(5):053902, Feb 2008.
- [27] Leach J. and Padgett M. J. Observation of chromatic effects near a white-light vortex. *New J. Phys.*, 5:154, 2003.
- [28] I. Marienko, J. Strohaber, and C. Uiterwaal. Creation of optical vortices in femtosecond pulses. *Opt. Express*, 13(19):7599–7608, 2005.
- [29] J. Leach, G. M. Gibson, M. J. Padgett, E. Esposito, G. McConnell, A. J. Wright, and J. M. Girkin. Generation of achromatic bessel beams using a compensated spatial light modulator. *Opt. Express*, 14(12):5581–5587, 2006.

- [30] A. J. Wright, J. M. Girkin, G. M. Gibson, J. Leach, and M. J. Padgett. Transfer of orbital angular momentum from a super-continuum, white-light beam. *Opt. Express*, 16(13):9495–9500, 2008.
- [31] G. Gbur, T. D. Visser, and E. Wolf. Anomalous behavior of spectra near phase singularities of focused waves. *Phys. Rev. Lett.*, 88(1):013901, Dec 2001.
- [32] M. V. Berry. Coloured phase singularities. *New J. Phys.*, 4:66, 2002.
- [33] M. V. Berry. Exploring the colours of dark light. *New J. Phys.*, 4:74, 2002.
- [34] M. S. Soskin, P. V. Polyanskii, and O. O. Arkhelyuk. Computer-synthesized hologram-based rainbow optical vortices. *New J. Phys.*, 6:196, 2004.
- [35] M. V. Berry and M. R. Denis. Quantum cores of optical phase singularities. *J. Opt. A: Pure Appl. Opt.*, 6(5):S178, October 2004.
- [36] H. He, M. E. J. Friese, N. R. Heckenberg, and H. Rubinsztein-Dunlop. Direct observation of transfer of angular momentum to absorptive particles from a laser beam with a phase singularity. *Phys. Rev. Lett.*, 75(5):826–829, Jul 1995.